Characterization of an aberration corrector utilizing two electrostatic mirrors for a low-voltage scanning electron microscope

Master thesis

Léon van Velzen

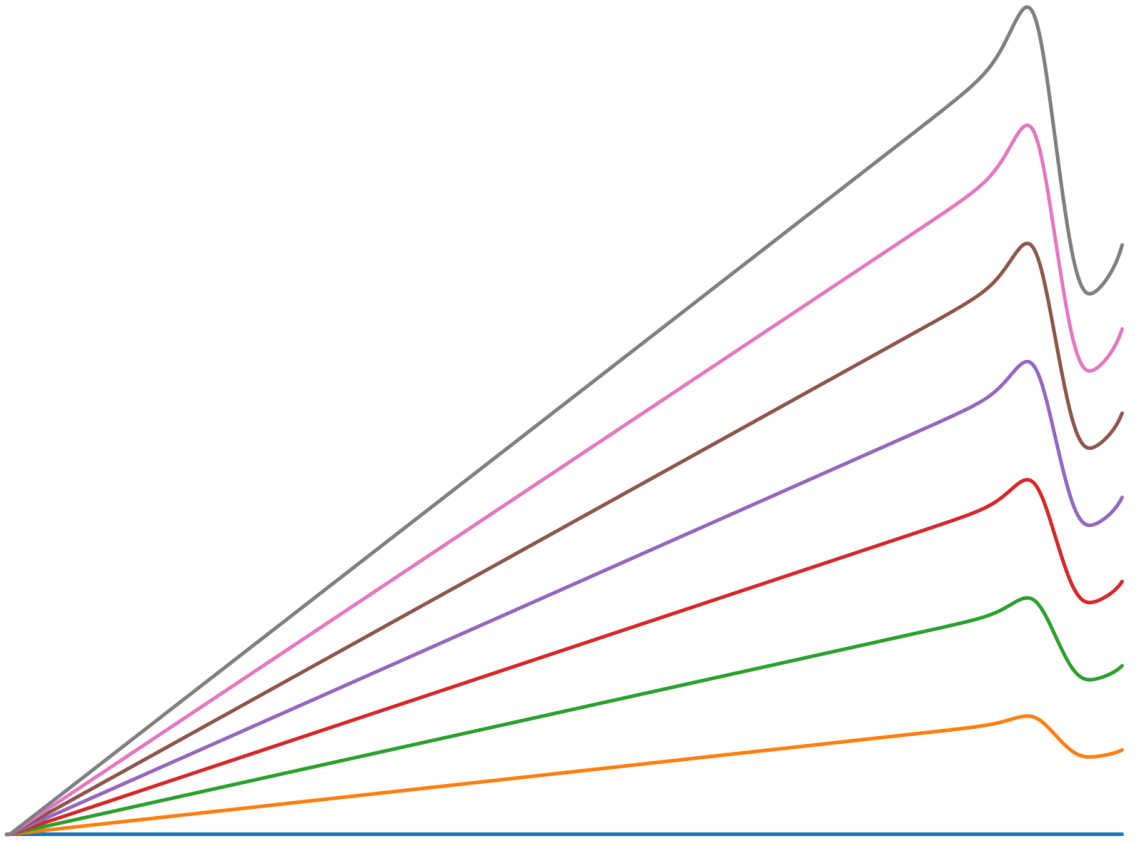

This page is intentionally left blank

Characterization of an aberration corrector utilizing two electrostatic mirrors for a low-voltage scanning electron microscope

Master thesis

Submitted in partial fulfillment
of the requirements for the degree of

Master of Science
in
Applied Physics

Author:	Léon van Velzen
Supervisors:	Diederik J. Maas Pieter Kruit
Assessment committee:	Diederik J. Maas Pieter Kruit Ali Mohammadi Gheidari Florian Bociort

To be defended on July 13, 2022

TU Delft Hitachi High-Tech

Abstract

The main factor limiting the resolution of scanning electron microscopes is the aberrations of the objective lens. Scherzer's theorem outlines the conditions under which correction of these aberrations can be achieved. One of the valid approaches is using electrostatic mirrors, although it has proven difficult to incorporate the mirrors in the beam path without introducing resolution limiting deflection aberrations. To limit the deflection aberrations it has been proposed to use MEMS technology to manufacture an aberration corrector employing only very small deflection angles (< 100 mrad). This aberration corrector is intended for low-voltage scanning electron microscopes and integrates two MEMS fabricated electrostatic mirrors. To study the optical properties of the corrector an implementation of the boundary element method is presented which uses a radial series expansion of the electric field to greatly improve the speed of ray tracing. Using this fast ray-tracing technique the aberrations of the electrostatic mirrors present in the design are characterized numerically. Next, it is shown mathematically that the corrector is capable of correcting the lowest order spherical and chromatic aberrations of the objective lens simultaneously. Theory is outlined on how to configure the corrector to achieve this simultaneous correction. An optical model of the microscope and the corrector is developed to assist in the experiments. The optical model can automatically compute the mirror excitation voltages needed to achieve the simultaneous correction of the spherical and chromatic aberrations while taking into account the current working conditions of the microscope. Furthermore, evaluation criteria to judge the quality of the electrostatic mirrors are presented and it is shown how they relate to the geometry of the mirror. Finally, experimental progress regarding the corrector is discussed. The lack of high-resolution images is hypothesized to be caused by a lateral misalignment of the two electrostatic mirrors, and experimental evidence is collected in support of this hypothesis. Despite this, the mirror excitation voltages that established the required focal length were found experimentally, and these voltages are shown to agree very well with the calculated values.

Contents

List of acronyms

SEM	Scanning Electron Microscope
LV-SEM	Low-Voltage Scanning Electron Microscope
TEM	Transmission Electron Microscope
MEMS	Micro Electro-Mechanical Systems
DMC	Double Mirror Corrector
CCP	Common Crossover Plane
BEM	Boundary Element Method
FEM	Finite Element Method
TEL	Top Einzel Lens
BEL	Bottom Einzel Lens
WD	Working Distance
EBE	Electrostatic/Magnetostatic deflector, see [1]

1

Introduction

Limitations of SEMs in the semiconductor industry

Scanning electron microscopes (SEMs) are widely used in the semiconductor industry for metrology, defect-review, and inspection. As feature sizes in semiconductor devices have been shrinking successfully for decades the resolution requirements on SEMs have become stricter [2]. As the smallest features in semiconductor devices now measure less than 10 nm the current generation of SEMs is reaching the limit of its capabilities [3]. The resolution of the SEM is mainly determined by the aberrations of the objective lenses used. The aberrations can be divided into chromatic aberrations, which are related to the inherent energy spread of the electron beam, and spherical aberrations, which manifest as a variation in focal length over the objective lens pupil (see figure 1.1).

Resolution loss of a SEM can also occur when the interaction volume of the electron beam in the sample is large [4]. For this reason, and also to limit damage from shrinking effects of the photoresist [3], it has become necessary to decrease the beam energy when using a SEM for metrology needs. However, decreasing the mean beam energy increases the relative energy spread of the electrons, which results in a larger chromatic blur from the objective lens and therefore in a loss of resolution. This problem would be overcome if the aberrations of the objective lens would be compensated. Correction of the chromatic aberrations would allow the SEM to retain its resolution even if the mean beam energy is decreased. Meanwhile, correction of the spherical aberrations would allow the beam angle to be increased, thereby decreasing the resolution limit imposed by diffraction effects. Simultaneous correction of the spherical and chromatic aberrations would allow the low-voltage scanning electron microscopes (LV-SEMs) to satisfy the metrology needs of the semiconductor industry even at future technology nodes.

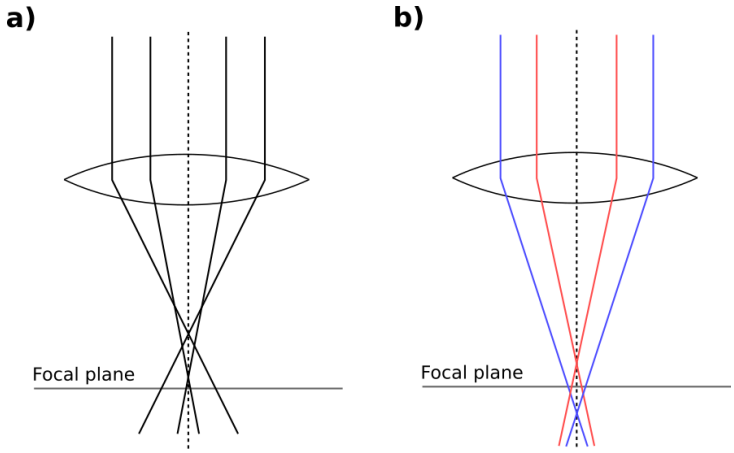

Figure 1.1: **a)** As a result of spherical aberrations the rays coming in further away from the optical axis are focussed too strongly. **b)** As a result of chromatic aberration the higher energy rays (blue) are focussed less strongly than lower energy rays (red). Because of the aberrations of the lens the rays do not intersect one another in the focal plane.

Scherzer's theorem and current attempts at aberration correction

Compensation of the aberrations in a SEM is difficult since Scherzer proved that under the following conditions the aberration coefficients are always of the same sign [5, 6, 7]:

1. All elements are rotationally symmetric.
2. Electric and magnetic fields are static.
3. There are no space charges or on-axis electrodes.
4. Potentials, fields, and their derivatives are smooth and continuous.
5. Electrons are never reflected.

Defying any of these conditions would allow for aberrations of standard electron lenses to be corrected, thereby improving the achievable resolution of the SEM. The most successful correctors now in use are multipole correctors, originally proposed by Scherzer himself [6, 8]. For generating negative aberrations multipole correctors invalidate condition (1), as they use non-rotationally symmetric elements. Multipole correctors have successfully been employed for correcting spherical aberrations in high voltage transmission electron microscopes (TEMs) [9, 10].

For LVSEMs correction of both the chromatic and spherical aberration is needed to significantly improve the imaging resolution. In 1995 Zach et al. [11] succeeded in correcting the chromatic and spherical aberration simultaneously using a multipole corrector, however, various issues need to be mentioned since they have prevented multipole correctors from reaching widespread use for LVSEMs today. First of all the tolerances on the components machined for multipole correctors and the electronic sources used are extremely strict. Also, electromagnetic multipole correctors offer only a short period of stable imaging as magnetic instabilities demand regular realignments. Purely electrostatic multipole correctors do not seem to suffer from these instabily issues [12]. Another drawback of multipole correctors is the large number of electrodes which need to be properly energized [12]. The correct setup of the multipole correctors for LVSEMs is complicated enough that automating this process has itself become a topic of research [13, 14].

Achieving aberration correction could also be achieved by defying any of the other conditions. Using non-static fields (defying condition 2) does not seem a very promising approach since very high-frequency power sources would be needed with very strict stability requirements. Using on-axis electrodes (defying condition 3) has been proposed in the literature [11, 15], as well as using space charge using extremely thin foils [16, 17]. Practical considerations have prevented their successful implementation.

The approach for aberration correction considered in this thesis employs electrostatic mirrors to generate aberrations with a negative sign (defying condition 5). The aberration-correcting properties of electron mirrors have been studied for a long time [18, 19, 20], but experimental progress has been frustrated by the problem of separating the reflected electron beam from the electron beam incident on the mirror [21, 22, 23]. One successful implementation of aberration correction using electrostatic mirrors is the SMART project [22]. The SMART project employs a 90° deflection to split the reflected beam from the incident beam [24], and the achieved resolution for spectroscopic applications is 2.6 nm [25]. Tromp et al. improved upon the SMART design by employing two magnetic deflector elements with the goal of adding symmetry to the system to nullify chromatic dispersion [26]. A resolution of 2 nm was achieved for low energy electron microscopy, while theoretically the resolution could be improved to 1 nm [27].

Implementation of the aberration corrector of the SMART project for a LVSEM was mentioned but to the author's knowledge, no published results are available. The challenge of using large deflection angles to separate the reflected and incoming electron beam is to prevent the deflection aberrations from nullifying any potential resolution improvements. Rempfer et al. proposed an electron microscope employing an electrostatic mirror for aberration correction while reducing the needed deflection angles [23]. Since the deflections occur in image planes the deflection aberrations are further reduced.

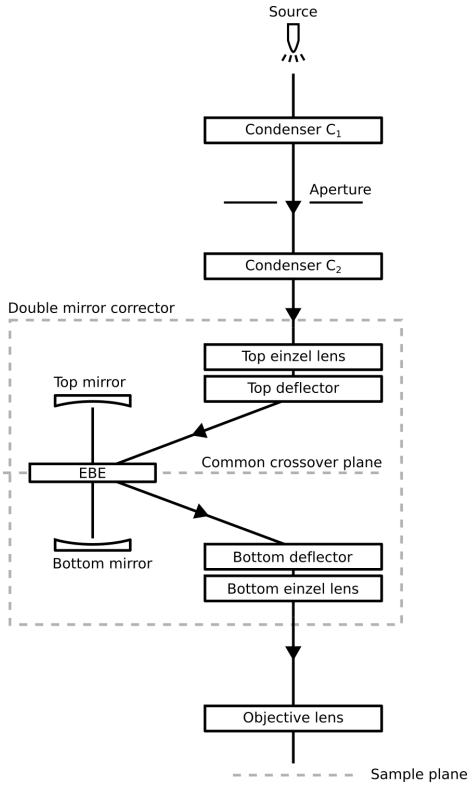

Figure 1.2: Schematic diagram of the relevant optical elements in the SU8030 microscope together with the double mirror corrector (DMC). Scan coils, stigmators and electron detectors are not included in the diagram. The DMC can be included in a conventional electron microscope since the beam exits the corrector in the same direction as it entered the corrector. The top column and both electrostatic mirrors focus the electron beam on the common crossover plane (CCP). The image is not to scale, the actual height of the DMC is less than 10 cm and the distance between the microscope axis and the mirror axis is less than a few millimeters.

Outline of the SEM and aberration corrector under study

The corrector under study in this thesis (and originally presented in [7]) uses micro-electro-mechanical systems (MEMS) to reduce the deflection angles more than previously possible. Before explaining the specifics of how the deflection angles have been reduced, let us first give a general outline of the design of the corrector. A schematic drawing of the corrector and the SU8030 microscope provided by Hitachi High-Tech Corporation (HHT) in which the corrector has been placed is shown in figure 1.2. The corrector uses a separate beam axis in which two electrostatic mirrors have been placed and is therefore named the Double Mirror Corrector (DMC). The electron beam exits the DMC in the same direction

as it entered the DMC and for this reason the corrector can be included in a conventional electron microscope. At the heart of the corrector lies the EBE unit, which is shown in more detail in figure 1.3. The EBE unit uses crossed electrical and magnetic fields to independently choose the deflection angle for an upward traveling beam and a downward traveling beam. The design and manufacturing of the EBE unit are detailed in [1].

The necessity of using MEMS becomes apparent when we mention the requirement that the mirror axis and the microscope axis should be distanced by only a few millimeters. This limits the deflection angles needed to less than 100 mrad which should keep the deflection aberrations under control. The deflection aberrations of the EBE unit are minimal if the beam width in the EBE is small. Therefore, the top column and the electrostatic mirrors focus the electron beam on the midplane of the EBE unit. This midplane is called the common crossover plane (CCP). Furthermore, a high degree of symmetry is present in the design, which implies that deflection aberrations (partially) cancel one another as argued in [7, 28].

The small distance between the mirror and microscope axis severely limits the opening diameter of the mirrors, which is currently chosen to be 80 to 250 µm. These small features require the very precise manufacturing capabilities offered by MEMS technology. For the manufacturing of the electrodes making up the mirror lithographic techniques matured by the semiconductor industry are used to achieve an accuracy better then 1 µm. The small distance between the mirror and microscope axis makes the electrodes of the mirror and deflectors encompass both the mirror and microscope axis. Therefore the electrodes are always manufactured with two holes to not obstruct either axis. As all the corrector elements need to affect the electrons on only one of the axis electrostatic shielding is added where appropriate. This is done using small hollow cylindrical metal pipes called *liner tubes*, which are at ground potential.

The two electrostatic mirrors present in the DMC consist of a stack of MEMS fabricated electrodes, with spacers between the electrodes to separate them at a well-defined distance. The mirrors are triode mirrors, since the electrons pass two electrodes before being reflected at the third electrode. A schematic cross-subsection of the electrostatic mirror is shown in figure 1.4. The electrodes of the mirror are stacked using a purpose-built stacker with the help of lithographic alignment markers on the electrodes with an accuracy better than 1 µm. The first electrode is grounded (like the microscope column) to provide a well-defined boundary condition. The second electrode is called the lens electrode, since it focuses the electron beam on the third electrode which is responsible for reflecting the electron beam. The third electrode is for this reason called the mirror electrode. The two arbitrary voltages that can be applied to the lens and mirror electrode provide two degrees of freedom to change the optical properties of the mirror. One degree of freedom is used to pick the appropriate focal length needed to focus the electron beam on the CCP. One degree of freedom is then left to choose from the available aberrations of the mirror. Since two mirrors are present each supplying one degree of freedom it should be possible to correct for both the chromatic and spherical aberrations. We will later see that the magnification of the bottom einzel lens provides another degree of freedom, meaning we can

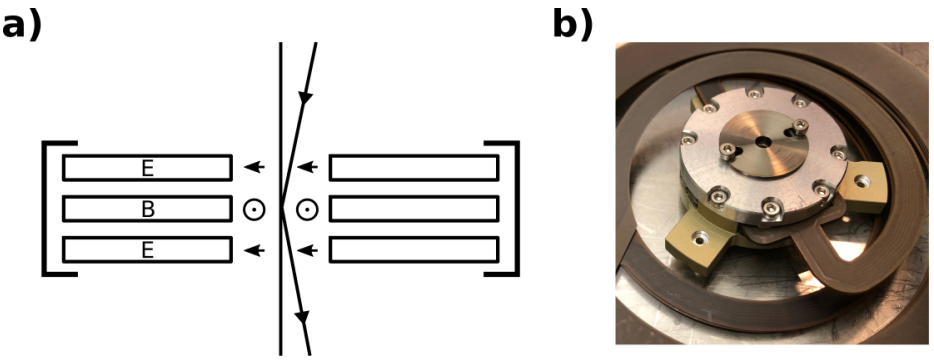

Figure 1.3: **a)** Schematic diagram of the EBE unit which uses alternating and crossed electrostatic and magnetostatic fields to provide a downward deflection angle which is different from the upward deflection angle. The direction of the electric and magnetic fields is shown in the image. Recall that the negative charge of the electron makes the beam deflect in the direction opposite to the electric field. **b)** Photograph of the casing of a constructed EBE unit. Both the microscope axis and the mirror axis pass through the central hole in the casing. Notice the flexible printed circuit board which transports the necessary voltages and currents to the EBE unit.

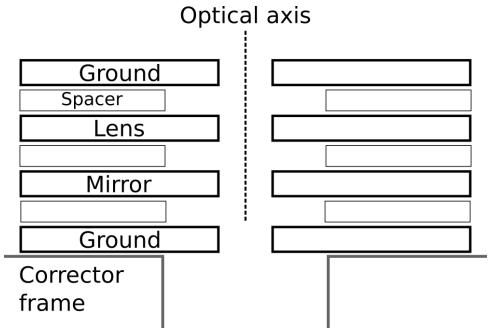

Figure 1.4: Schematic diagram of the triode mirror used in the DMC. The circular apertures in the electrodes are etched using lithographic techniques which results in very little surface roughness. The electrodes of the mirror are stacked using a purpose-built stacker with the help of lithographic alignment markers on the electrodes with an accuracy better than 1 µm. The electrodes in the stack are glued together, after which the mirror itself is glued to the corrector frame.

correct for both the spherical and chromatic aberrations while exciting both mirrors with the same voltages.

The design of the DMC is complicated enough to require extensive computer modeling to completely characterize its behavior. Some numerical results are available in the original

publication of the design [7], but many questions remain that could be answered by numerical techniques. The goal of this thesis is to find good models of the corrector, and by doing so establish how the corrector should be operated to improve the resolution of the SEM.

To find the aberrations of the electrostatic mirrors, different approaches can be taken. In the original publication of the design [7] aberration integrals were used, these allow the aberration coefficients to be calculated from the knowledge of the electrostatic potential along the optical axis, the derivatives of the potential along the optical axis, and the two paraxial rays. Standard numerical techniques like the finite element method (FEM) or boundary element method (BEM) still need to be employed to find the electrostatic potential and its derivatives. In [29] aberrations of different electrostatic mirrors are calculated by using the FEM and real (i.e. non-paraxial) ray tracing (see also [30]). In this thesis, we have chosen to use the BEM and real ray tracing to produce the numerical results. A comparison between the computational method used here and the methods from the literature is made in chapter 2.

Thesis outline and research questions

In chapter 2 we discuss how to efficiently calculate the aberration coefficients of the electrostatic mirrors. We shortly discuss the boundary element method (BEM) which is already thoroughly described in the literature. Specifically for this thesis, a Python implementation of the BEM has been developed to solve for the electrostatic fields of the mirrors. It was found that naive ray-tracing using the BEM was very time-consuming if high accuracy is needed. For this reason, a novel interpolation technique is presented to greatly increase the speed of the field calculations. Results of the electrostatic solver and the ray tracer are compared with the literature to show that the software produces very accurate results. A comparison is made between the computational method chosen here and those used previously to study electrostatic elements [7, 29, 30]. The software used for the calculations is publicly available as open-source software and is expected to answer more research questions in the field of charged particle optics in the future.

In chapter 3 the computational techniques elaborated in chapter 2 are used to find the aberration coefficients for the mirror geometry that is currently installed in the DMC. It is shown numerically how the aberration coefficients change with the focal length of the mirror. Also, the higher-order aberration coefficients of the mirror are presented. These are not used in later chapters but are useful to ensure the higher-order aberrations of the mirrors are small enough to not degrade the function of the aberration corrector.

In chapter 4 we go into detail on how the aberration corrector should be operated. Formulas are derived which relate the aberrations of the DMC to the aberrations of the electrostatic mirror used. Also, we discuss what aberrations we expect to need from the DMC to compensate for the aberrations of the objective lens. Using the theory in this chapter the 'aberration matching condition' is derived, which is a constraint which needs to be satis-

fied in order to open up the possibility of correcting both the chromatic and spherical aberrations simultaneously. The main contribution of this chapter is the 'aberration matching procedure' which precisely details how the DMC should be configured to achieve correction of both the chromatic and spherical aberrations when the aberrations of the objective lens are known.

In chapter 5 we consider the design of the electrostatic mirrors. A certain number of evaluation criteria are presented which allow us to judge the quality of the electrostatic mirrors. Starting from a reference design a few geometrical parameters are varied and their effect on the evaluation criteria is calculated. Furthermore, a tetrode mirror is constructed by adding an electrode to the reference design, and the effect of exciting this auxiliary electrode on the evaluation criteria is systematically studied. A conclusion is made about which geometrical parameters of the mirrors have the largest effect on their optical properties. The data presented in chapter 4 will be useful when a novel mirror design is considered.

In chapter 6 details are shared about the experimental progress that has been made during the writing of this thesis. The chapter contains an alignment procedure that is paramount to successfully embed the corrector in the beam path of the microscope. Unfortunately, it has been found that as of yet no high-resolution images can be obtained while operating the DMC. Some experimental evidence is obtained for a hypothesis explaining the reduced imaging quality of the DMC. The lack of high-resolution images has so far prevented the experimental determination of the aberrations produced by the DMC. Still, it has been possible to establish the relevant excitation voltages of the electrostatic mirrors and these are compared with the calculations of the previous chapters.

In appendix A an optical model of the SU8030 microscope is presented. Hitachi High-Tech Corporation has shared enough implementation details of the microscope to precisely map the settings in the software interface to the working conditions of the microscope[1]. While experimenting the optical model allows for the immediate and interactive calculation of the conditions inside the microscope such as the beam angle in the corrector, the aberrations of the objective lens at the given working distance, and the expected resolution at the sample plane. The aberration matching procedure from chapter 4 has also been implemented and fully automized in the model. This means that the necessary corrector configuration (such as mirror voltages) to achieve simultaneous correction of spherical and chromatic aberration can instantaneously be computed. Some calculations from the optical model are verified experimentally.

[1] Care has been taken to not include any sensitive information from Hitachi High-Tech Corporation in this thesis.

2

Computational model

To find the aberrations of the electrostatic mirror we follow a three-step procedure:

1. Solve for the electrostatic potential as a function of the voltages on the electrodes.
2. Trace electrons through the electrostatic potential.
3. Perform a fit to the deviations from optimal focusing.

We discuss these steps in detail in the next sections. We end the chapter with a comparison between the computational method employed here and those used previously in the literature [7, 29, 30]).

2.1 Solving for the electrostatic potential

To find the electrostatic potential we use the Boundary Element Method (BEM) [31, 32]. In the boundary element method, we divide the boundaries of the electrodes in N_{lines} number of line elements. The charge on each line element is considered as the unknown quantity that should be solved for. A given line charge on one of the line elements contributes to the electrostatic potential at the position of another liner element. Since at a certain line element the potential contributions of all other line elements must sum to the voltage of the corresponding electrode, every line element adds one constraint on the charges of the line elements. These constraints can be expressed in a N_{lines} by N_{lines} matrix A in which the matrix element A_{ij} is given by the potential contribution of line element j at the position of line element i. Expressing the applied voltages at every line element as a vector ϕ we can solve the linear system $A\rho = \phi$ to find the line charges ρ.

The formula for the potential contributions (the matrix elements) can be derived by considering the integral form of Poisson's equation in an axisymmetrical coordinate system

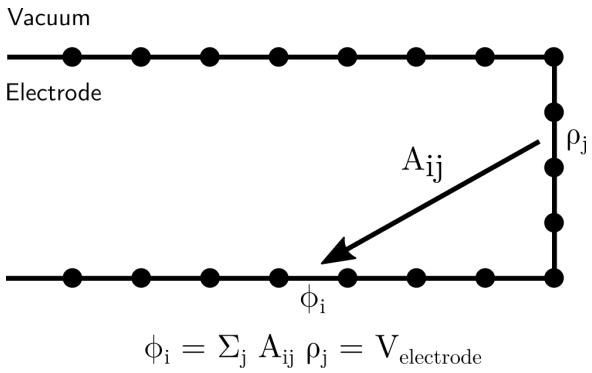

Figure 2.1: In the Boundary Element Method (BEM) we divide the boundary of an electrode in a large number of line elements. A linear system is constructed in which the matrix elements represent the potential contribution of a line element at the position of another line element.

(see [31] for the derivation). The result is

$$\phi(r_0, z_0) = \frac{1}{\pi\epsilon_0} \int \frac{\rho_j K(t) r}{\sqrt{(r + r_0)^2 + (z - z_0)^2}} ds \tag{2.1}$$

where

$$t(r_0, z_0) = \frac{4 r r_0}{(r + r_0)^2 + (z - z_0)^2}$$

This formula expressed the potential contribution at $\mathbf{x}_0 = (r_0, z_0)^T$ in an integration over the line element at $\mathbf{x} = (r, z)^T$ with line charge ρ. The function $K(t)$ is the complete elliptic integral of the first kind and results from our assumption of axial symmetry. ϵ_0 is the permittivity of vacuum.

Once the charges ρ have been determined by solving the linear system a summation of the contributions of all line elements (given by formula 2.1) can be used to determine the potential at any point in space $\mathbf{x}_0$.

Practical considerations

The matrix A in the resulting linear system is a dense, but small matrix. The number of rows and columns of the matrix in this work is usually on the order of $N_{\text{lines}} \sim 10^4$. Since the matrix is dense and the accuracy of the computed line charges is very important a direct solver is used to solve the linear system.

In practice, it is found that constructing the matrix A has a higher computational cost

z/diameter	D. Edwards, Jr [33] (V)	Relative accuracy
0.0	5.00000...	3×10^{-7}
0.2	2.5966375	6×10^{-6}
0.4	1.1195606	7×10^{-6}
0.6	0.44487400	-3×10^{-7}
0.8	0.17200281	-2×10^{-5}
1.0	0.065954697	-7×10^{-5}

Table 2.1: Accuracy of the implementation of the Boundary Element Method (BEM) in this work is determined by using values from [33] for an electrostatic reference problem which are thought to be accurate to better than 10^{-8}. The number of line elements is chosen such that the BEM solution step takes one minute on a consumer grade laptop.

than solving the resulting linear system. The reason for this is the integration present in formula 2.1. This numerical integration needs to be performed for every matrix element A_{ij}. To decrease the time needed to calculate matrix A we can consider the integrand to be approximately constant whenever the contributing line element is far away from the line element at which the contribution is calculated. In this case, we use

$$\phi(r_0, z_0) = \frac{1}{\pi \epsilon_0} \frac{\rho_j K(t(r = r_m, z = z_m)) r_m}{\sqrt{(r_m + r_0)^2 + (z_m - z_0)^2}} \Delta s$$

Where r_m, z_m are the coordinates of the center of the contributing line element with length Δs.

Another important point regarding the integration is the apparent singularity whenever calculating A_{ii}. When calculating the potential contribution to the position of a line element by the line element itself formula 2.1 contains a singularity at the center of the line element. The integration however is convergent as long as care is taken not to step into the singularity. The most straightforward solution is to take an even number of equally spaced integration points along the line element.

Finally, it's advantageous to solve for the quantity $\frac{\rho}{\pi \epsilon_0}$ instead of the line charges ρ to prevent the software from working with extremely small floating point quantities.

Validation

To validate the current implementation of the boundary element method we make a comparison with values computed in the literature. For this, we use the simple reference problem presented in [33]. In this work, the potential of an electrostatic lens consisting of two axisymmetrical tubes with thick walls is computed along the optical axis. The accuracy of the published values of the electrostatic potential is thought to be better than 10^{-8}. The comparison is shown in table 2.1. There is good agreement between the values

computed in this work and the literature values. This comparison implies that the relative error (computed as $\frac{\phi}{\phi_{\text{reference}}} - 1$) on the electrostatic potential computed in this work is better than 10^{-4}.

2.2 Electron tracing

To trace electrons through the electrostatic mirror we need a procedure to evaluate the electric field at any point in space and a time iteration method.

To compute the electric field at $\mathbf{x}_0 = (r_0, z_0)^{\mathrm{T}}$ we could take the derivative of 2.1 with respect to r_0 and z_0 and sum over all the line element contributions. This is the standard approach in the boundary element method. The derivatives are given by

$$E_r = -\frac{\partial \phi}{\partial r_0} = \frac{-1}{\pi \epsilon_0} \int \frac{\rho r}{2 r_0} \frac{\left(1 + \frac{2 r r_0}{(r-r_0)^2 + (z-z_0)^2}\right) E(t) - K(t)}{\sqrt{(r + r_0)^2 + (z - z_0)^2}} ds \tag{2.2}$$

$$E_z = -\frac{\partial \phi}{\partial z_0} = \frac{-1}{\pi \epsilon_0} \int \frac{\rho r (z - z_0) E(t)}{\left((r - r_0)^2 + (z - z_0)^2\right) \sqrt{(r + r_0)^2 + (z - z_0)^2}} ds \tag{2.3}$$

where $E(t)$ is the complete elliptic integral of the second kind.

This procedure works well as long as only a small number of electrons need to be traced. The computational cost of this approach is large since for every field evaluation an iteration over all line elements needs to be performed. For line elements that are close to the current position of the electron the numerical integration also needs to be performed explicitily. Since for this work a large number of electrons needs to be traced ($> 10^6$) an alternative method needs to be considered.

To speed up the field evaluation, we make use of the radial series expansion formula for the electric field [34]:

$$E_r(r, z) = \frac{r}{2} \phi^{(2)}(z) - \frac{r^3}{16} \phi^{(4)}(z) + \frac{r^5}{384} \phi^{(6)}(z) - \frac{r^7}{18432} \phi^{(8)}(z) + \cdots \tag{2.4}$$

$$E_z(r, z) = -\phi^{(1)}(z) + \frac{r^2}{4} \phi^{(3)}(z) - \frac{r^4}{64} \phi^{(5)}(z) + \frac{r^6}{2304} \phi^{(7)}(z) + \cdots \tag{2.5}$$

Where $\phi^{(n)}(z)$ is the n-th derivative with respect to z of the potential along the optical axis. By precomputing the derivatives of the potential at a number of points along the optical axis, a field evaluation need only to interpolate the derivatives along the optical axis to the current z coordinate of the electron and evaluate the series expansion. Computing the derivatives is computationally costly but need only to be done once per electrode for a

Angle (rad)	Formula (4) from [36] (mm)	Computed (mm)	Relative accuracy
0.0	10.000...	9.99986	1×10^{-5}
0.05	9.95017	9.95008	9×10^{-6}
0.1	9.80263	9.80255	8×10^{-6}

Table 2.2: To judge the accuracy of the naive BEM ray-tracing method implemented for this work we consider the spherical capacitor described in [36]. An exact formula is presented in this publication which gives the intersection with the z-axis of an electron initially at an angle relative to the median trajectory. In this work the concentric spheres making up the spherical capacitors have radii 7.5 mm and 12.5 mm and therefore formula (4) from [36] needs to be multiplied by a factor of 10 to get the correct values. The relative accuracy is 1×10^{-5} or better.

given geometry since superposition can be used to find the derivatives when the voltages on the electrode change.

To compute the derivatives of the potential along the optical axis the analytical derivatives of formula 2.1 can be used. However, the expressions for the derivatives are so elaborate that they can only be found using a computer algebra system. In practice, it is found that the expression for the fifth derivative contains so many terms that numerical accuracy issues arise. Therefore up to the fourth derivative is computed analytically while higher-order derivatives are computed using a high order finite difference formula starting from the values of the fourth derivative. Using this approach with a sampling of 150 points per mm on the optical axis it is found that up to and including the eighth derivative can be computed without visible numerical noise.

For the time-stepping method we use an adaptive Runge-Kutta-Fehlberger method (RK4(5), see [35]).

Validation

To estimate the accuracy of the electron tracing, we consider two different benchmark tests both taken from [36]. The first benchmark judges the accuracy of the naive BEM ray tracing in which we iterate over all line elements every time the electric field needs to be computed. The geometry used is the spherical capacitor, consisting of two concentric spheres of radius 7.5 mm and 12.5 mm at potentials 5/3 V and 3/5 V respectively. The median trajectory of a 1 eV electron will travel through the middle of the radial gap and intersect the z-axis at 10 mm. If the electron initially has an angle with respect to this median trajectory the intersection with the z-axis is given by formula (4) of [36]. The result of the comparison with this formula is shown in table 2.2. A relative accuracy of 1×10^{-5} or better is achieved.

In the second benchmark taken from [36] we consider the accuracy of the ray-tracing using the fast field evaluation scheme elaborated in the previous section. The previous

benchmark problem cannot be used since the electrons do not travel along the z-axis, which is a requirement for the interpolation scheme to work. Instead, we note that in [36] values are presented for the intersection points with the optical axis for electrons traveling through a double cylinder lens with zero wall thickness. With the fast ray-tracing method of this work, these intersection points can be reproduced with a relative accuracy of $\sim 4 \times 10^{-4}$. However, since the values in [36] are only noted with five significant digits it is unclear whether this inaccuracy stems from the values in [36] or from the software used in this work. In the validation of the next section, we will see that the fast ray-tracing method can reproduce aberration coefficients from the literature with a relative accuracy up to 3×10^{-6}, proving the method to be very accurate.

2.3 Fitting procedure for the aberration coefficients

Following the literature, we define our aberrations in terms of the r coordinate of the intersection of the electron trajectory with the focal plane. We refer to this deviation from perfect focusing with Δr to emphasize the fact that it's defined relative to a non-aberrated electron trajectory for which $\Delta r = 0$. See figure 2.2 for the coordinate system used.

The deviations from perfect focus for an axisymmetrical system can be a result of the angle that the electron makes with the optical axis at the start of its trajectory. This angle causes the electron to sample the electric field of the lens or mirror far away from the optical axis where the resulting focal length of the lens or mirror might be slightly different. Another cause of aberrations is an energy difference the electron might have relative to the mean energy of the electron beam. As the focusing of the lens or mirror is usually optimized for the mean beam energy an electron at different energy might follow a different trajectory.

Once a number of electrons at different initial angles and kinetic energies are traced the resulting Δr values can be fitted to a two-dimensional polynomial to find the aberration coefficients C_{ij}:

$$\Delta r = \underbrace{-\sum_{i=1,i\text{ odd}} C_{i0}\alpha^i}_{\text{spherical}} + \underbrace{\sum_{i,j=1,i\text{ odd}} C_{ij}\alpha^i \left(\frac{\Delta E}{E}\right)^j}_{\text{chromatic}} \qquad \text{(i is odd)} \tag{2.6}$$

As a consequence of the axial symmetry around the optical axis Δr needs to be an odd function of the angle and therefore only odd powers of α are present in the polynomial fit. Furthermore $C_{10} = 0$ when the deviations are measured in the focal plane (as they should). The aberrations are named spherical aberrations when they depend on the initial angle only or chromatic aberrations when they are dependent on the electron energy. As standard in the literature, we define the convenient shorthands $C_s = C_{30}$ and $C_c = C_{11}$ for

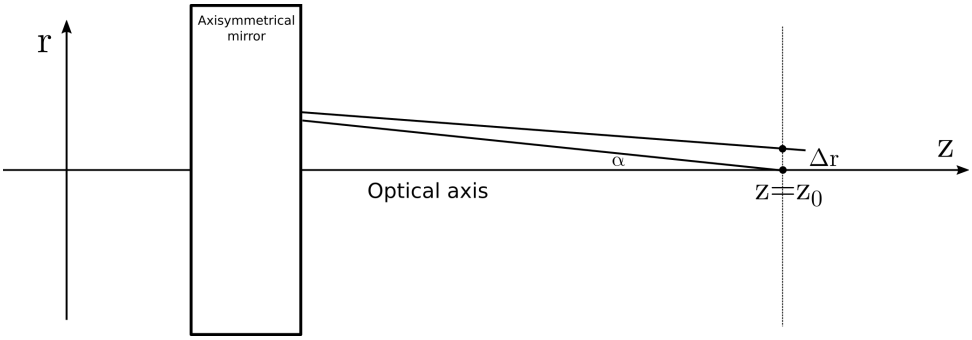

Figure 2.2: Axisymmetric coordinate system used for all geometries in this work. In the schematic drawing, an electron starts from the focal plane (dotted line) and is reflected back to the same position. As a result of aberrations, a deviation of Δr is measured in the focal plane. Note that $\Delta r > 0$ for an underfocus (situation drawn) and $\Delta r < 0$ for an overfocus (when $\alpha > 0$).

the lowest order spherical and chromatic aberrations respectively.

A comment should be made about the chosen signs in formula 2.6. Scherzer's theorem implies whether an aberration of the objective lens will lead to an overfocus or an underfocus. The signs in the preceding formula are chosen in such a way that the coefficients will always be positive for an objective lens. To be more specific:

Box 2.3.1. Sign convention of the aberration coefficients

- A positive spherical aberration will lead to an overfocus
- A positive chromatic aberration will lead to an underfocus for electrons with $\Delta E > 0$

Since an overfocus corresponds to a negative Δr value (when $\alpha > 0$), a minus sign is added to the spherical terms in formula 2.6 to have positive spherical aberration coefficients.

Validation

The computation of aberration coefficients using the described method for obtaining the electric potential and tracing the electron trajectories is validated using values from the literature. For this, we consider the diode mirror studied by D. Preikszas and H. Rose [37]. In the cited work the aberration coefficients are obtained using a combination of analytical and numerical techniques. The accuracy is claimed to be six significant digits on the low order aberrations and decreases to three significant digits for the fifth-order spherical aberration. The comparison with values computed in this work is shown in table

Aberration coefficient	D. Preikszas [37]	Relative accuracy
$C_c = C_{11}$	0.187461r	3×10^{-6}
$C_s = C_{30}$	-0.61629r	3×10^{-6}
C_{12}	-0.0777r	2×10^{-4}
C_{31}	8.669r	7×10^{-3}
C_{50}	-169.63r	5×10^{-3}

Table 2.3: Comparison of aberration coefficients calculated in this work with those from the literature [37]. The variable r is a parameter of the reference geometry and in this work chosen as $r = 5\,\text{mm}$. Notice that the relative accuracy of some coefficients is limited by the number of significant digits presented in [37].

2.3. The relative accuracy is a remarkable 3×10^{-6} for C_{11} and C_{30} but drops to 5×10^{-3} for the higher-order coefficients.

2.4 Comparison with computational methods from the literature

Let us for a moment discuss why the effort has been undertaken to develop a new software library to compute the aberrations of the electrostatic mirrors. Alternatively, we could have used so-called aberration integrals [7, 34]. These are analytical expressions for the aberration coefficients in terms of the potential along the optical axis, the derivatives of the potential along the optical axis, and the two paraxial rays. The advantage of this method is the possibility to avoid writing large amounts of custom software, as the needed axial potential can be exported from commercial software packages. However, the main drawback is the complexity of the aberration integrals in the case of mirrors [7, 38]. Also, the method lacks generality, as for any optical property a new complicated analytical expression needs to be derived.

For the previous reasons, real (i.e. non-paraxial) ray tracing is the preferred method. In [29] the FEM method is combined with real ray tracing to find the aberration coefficients of different electrostatic mirrors. However, the BEM method used here is inherently more accurate at a given computation time (see [36]) since only the boundaries need to be meshed instead of the entire geometry. Also, in [29] only on the order of 10^3 electrons have been traced, whereas the number of electrons traced for this work is orders of magnitude larger. Therefore, the time needed per traced electron is an especially important property. The usual drawback of the BEM method is the slow particle tracing since an iteration needs to be made over all the line elements for every field evaluation. But this drawback is avoided by using the field evaluation technique presented in section 2.2. This technique ensures a field evaluation on the order of 0.5 µs and an electron trace on the order of 4 ms on consumer-grade hardware.

Another more practical advantage of custom software is the possibility of completely automating the computation of the quantities of interest. Also, custom software opens the possibility of publishing the software in an open-source fashion. This allows for better reproducibility of this work and also allows other researchers to extent the software to suit their specific needs. In conclusion, we claim the electrostatic solver presented here improves upon the previously available methods. The solver possesses the generality of real ray tracing, the accuracy of the BEM, and the usual advantages of an open-source modern software implementation. Also, the employed field evaluation method allows for very fast ray traces.

3

Aberrations of Dohi's mirror design

Having described the necessary computational techniques to analyze an electrostatic mirror we now turn our attention to the mirror design currently integrated into the aberration corrector. This mirror design is a practical implementation of the design presented in [7].

3.1 Mirror geometry

The geometry of the current mirror design is shown in figure 3.1**a**. The ground electrodes at the top and bottom of the design make sure that proper boundary conditions are available for the BEM. The design further employs a mirror electrode whose voltage is always more negative than the energy of the electron beam. This ensures the electrons are properly reflected. Under normal operating conditions the turning point of the electrons is close to the upper surface of the mirror electrode. The lens electrode in the mirror allows tuning the aberrations of the mirror. How the 3D geometry is translated to a BEM model is shown in figure 3.1**b**. The colored boundaries are broken up into smaller line elements and used in the BEM. The grey boundaries have no prescribed voltage and are ignored. The total number of line elements used for computing the electrostatic potential is on the order $N_{\text{lines}} \sim 10^4$. By translating the 3D geometry to a 2D geometry we greatly reduce the computational cost but make the compromise of not computing the impact of the grounded liner tubes on the electron trajectories. In chapter 5 we consider a perturbation method to estimate the impact of the liner tubes.

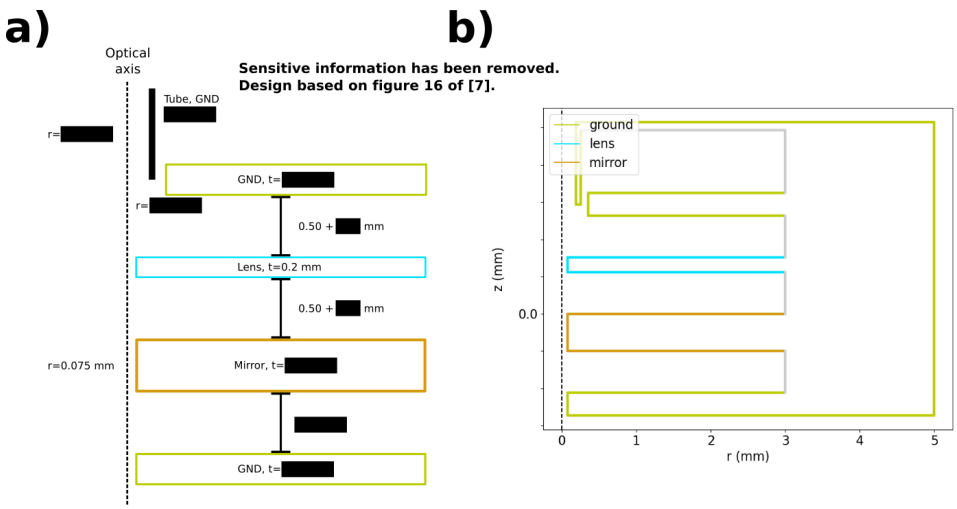

Figure 3.1: **a)** Schematic drawing of the mirror geometry currently used in the Double Mirror Corrector (DMC). The mirror is rotationally symmetric around the optical axis. The spacers between the electrodes are 0.5 mm thick but [redacted] µm has been added to account for the glue layers between the electrodes and the spacers. The grounded tube at the top of the geometry shields the incoming electrons from electrostatic fields from the microscope axis. **b)** Outline of the electrostatic mirror when used for the Boundary Element Method (BEM). The potential on the colored boundaries is specified and equal to the voltages applied to the electrodes. The grey boundary elements are ignored. Notice that a grounded (0 V) boundary encompasses the lens and mirror electrodes on the right. This boundary ensures the potential is zero above the upper grounded electrode and is necessary for reasons of numerical accuracy. The coordinate system has been chosen such that the top of the mirror electrode is at $z = 0$ mm.

3.2 Mirror focal lengths

In the presented mirror design we are free to apply a voltage on the lens electrode and a voltage on the mirror electrode. The only constraint is that the voltage on the mirror electrode is more negative than the beam energy to ensure that the electrons are reflected. When this condition is not met the mirror functions as an electrostatic lens, which is useful in an experimental setting to achieve correct beam alignment in the aberration corrector.

To calculate the aberrations of the mirror it is necessary to first find the relation between the focal length of the mirror and the voltages applied to the electrodes. To elucidate this relation first a global scan of the focal length is attempted. For the global scan, a large voltage range for both the mirror and the lens electrode is considered and for each possible voltage combination, an attempt is made to find the focal length of the mirror. For many voltage combinations, the mirror has no focusing behavior or the focal length

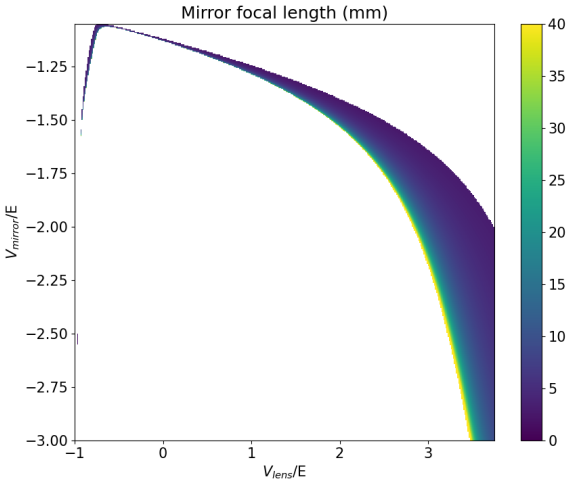

Figure 3.2: Global scan of the focal length of the electrostatic mirror shown in figure 3.1. To generalize the result, the applied voltages (horizontal and vertical axis) have been normalized to the mean beam energy. Locations in the image are left blank when the method described in the text failed to determine the focal length. From the resulting image, it can be seen that the mirror is very sensitive to changes in the voltage applied to the mirror electrode whenever the voltage on the lens electrode is small. Also note that, for a given focal length, the voltages on the mirror electrode can be considered a single-valued function of the voltage on the lens electrode.

is outside the range of the numerical method used. In these cases, the focal length is left unspecified. The focal length is determined by tracing an electron starting on the optical axis at a distance $z = z_0$ from the mirror electrode and making an initial angle of $\alpha = 0.05\,\text{mrad}$ with respect to the optical axis. This small angle ensures that aberrations do not play a significant role. A Newton iteration is performed on the distance $z = z_0$ until the reflected electron intersects the optical axis at the same z coordinate it started from (z_0). The focal length of the mirror is then given approximately by $f = \frac{z_0}{2}$.

In figure 3.2 the result of the global scan is shown. The voltages are normalized to the beam energy to generalize the result to any beam energy. It can be seen that at small or negative lens voltages the variation in focal length (the different colors in figure 3.2) are confined to a very small extent in the y-direction. This means, that at small or negative lens voltage, a small change in the voltage of the mirror electrode will result in a large change in the focal length of the mirror. This implies that the mirror is very sensitive to voltage deviations on the mirror electrode. Figure 3.2 consists of 400^2 pixels and is computed by considering all combinations of 400 different lens and mirror electrode voltages. Since a few electron traces are needed to accurately determine the focal length of the mirror a total of 10^5 to 10^6 electron traces have been performed in creating this image. It now becomes clear that

the fast electron tracing method presented in section 2.2 is crucial to perform such an elaborate mirror characterization. Using the fast electron tracing technique the presented image can be generated in less than an hour on consumer-grade hardware. From figure 3.2 it can be seen that for a fixed focal length the mirror electrode voltage is a single-valued function of the lens electrode voltage. Therefore the mirror electrode voltage and the aberration coefficients can always be plotted as a function of the lens electrode voltage as long as the focal length has been fixed.

3.3 Aberration coefficients

From figure 3.2 we can extract the approximate electrode voltages needed to achieve a certain focal length. For a number of lens voltages we use this approximate mirror voltage as the starting value, and then use Newton's method on the mirror voltage to achieve $C_{10} = 0$ in a chosen focal plane. This enables us to find the electrode voltages needed for a certain focal length with high accuracy. Having found the correct electrode voltages for the target focal length, we can use the techniques from the previous chapter to find the aberration coefficients. The result of this procedure is shown in figure 3.3. It can be seen that C_{11} and C_{30} are both negative, which is a prerequisite for aberration correction. Also, if we assume reasonable order of magnitudes for the beam angle and the energy spread $\alpha \sim 10^{-4}$, $\frac{\Delta E}{E} \sim 10^{-3}$ it is easy to calculate that the higher-order aberration coefficients will have negligible impact. The magnitudes of C_{11} and C_{30} are much larger than for conventional objective lenses. However, the aberrations of the mirrors will have been demagnified by the objective lens before reaching the sample plane. We will see in chapter 4 how the bottom einzel lens can be used to make sure the magnitude of the mirror aberrations match those of the objective lens at the sample plane.

From figure 3.3 it can be seen that the aberration coefficients increase drastically as the focal length is increased. This can be explained by the fact that at a fixed angle, an electron starting farther away from the mirror will reach the mirror at a larger distance from the optical axis. This means that a larger volume of the electromagnetic potential is sampled by the electron beam. The electron beam will therefore encounter more imperfections in the electrostatic potential of the mirror.

To explain the characteristic shape of the aberration coefficients as a function of lens voltage, a number of electron traces for the case of a focal length $f = 5\,\text{mm}$ are plotted in figure 3.4. It can be seen that at a negative lens voltage the lens electrode functions as an electromagnetic lens, preventing the electrons from moving far from the optical axis into the electrostatic mirror and thereby suppressing the aberrations. As the lens electrode voltage is zeroed, this lens effect vanishes, and the electron is free to travel far away from the optical axis. The result is very large aberration coefficients as can be seen in figure 3.3. Finally, as the lens electrode voltage is increased the lens electrode again acts as an electromagnetic lens and starts to push the electron towards the optical axis, reducing the aberrations.

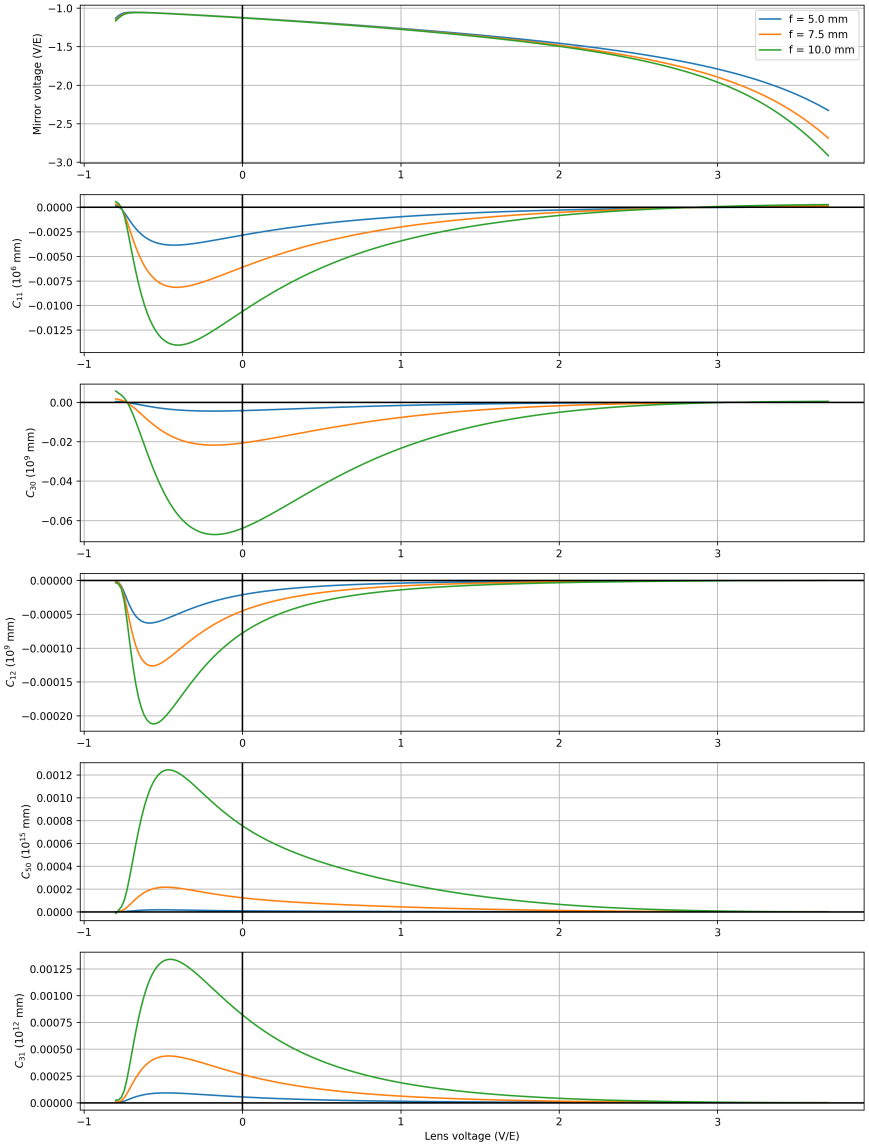

Figure 3.3: Characterization of the electrostatic mirror shown in 3.1 for focal lengths $f = 5, 7.5, 10$ mm. Only certain voltages on the lens and mirror electrode give rise to the relevant focal lengths. A Newton iteration on the mirror electrode voltage ensures that accurate focusing is achieved ($C_{10} \approx 0$). The relation between the mirror and lens electrode voltages is shown in the first graph. Note that the voltages are normalized to the mean beam energy to generalize the result. In the subsequent graphs, the aberration coefficients (as defined in equation 2.6) that correspond to the given mirror and lens electrode voltages are plotted. The aberration coefficients are computed for electrons starting at $z_0 = 2f$ which are reflected back to the focal plane at $z = z_0 = 2f$. If we assume reasonable order of magnitudes for the beam angle and the energy spread $\alpha \sim 10^{-4}$, $\frac{\Delta E}{E} \sim 10^{-3}$ we can calculate that the higher-order aberration coefficients will have negligible impact. The magnitudes of C_{11} and C_{30} are much larger than for conventional objective lenses. We will see in chapter 4 how the magnifications of the bottom einzel lens and the objective lens will ensure that the mirror aberrations match those of the objective lens at the sample plane.

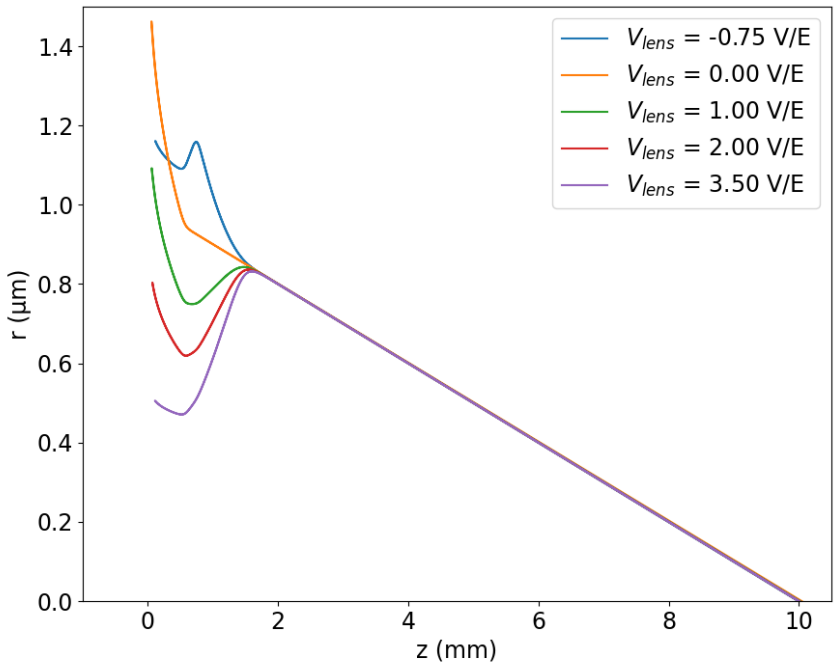

Figure 3.4: Characteristic electron traces for a number of different lens electrode voltages for the mirror shown in figure 3.1. The voltages are normalized by the mean beam energy. The mirror electrode voltage is chosen such that the focal length is $f = 5$ mm. This ensures that the electrons starting from $z_0 = 10$ mm are reflected back to the starting position. For lens electrode voltages that are large in absolute value the lensing effect is strong, causing the electrons to sample a smaller volume of the electrostatic field of the mirror. This suppresses the aberrations, as can be seen in figure 3.3.

4

Matching corrector aberrations with the objective lens

The main contribution of this chapter is a procedure for achieving optimal matching of the lowest order chromatic and spherical aberrations of the DMC to those of the objective lens. This procedure uses the bottom einzel lens (BEL) as a transfer lens. In support of this procedure, we first derive the so-called 'matching condition' which is a constraint the mirror aberration coefficients need to satisfy in order to allow simultaneous correction of the chromatic and spherical aberrations (and which cannot be satisfied by tweaking the BEL magnification). We also derive theory on how the aberration coefficients of the mirrors change when the object or image distance deviates from the CCP and we derive an elegant formula for expressing the aberrations of the DMC in terms of the single mirror aberrations.

4.1 Aberration coefficients as a function of focus positions

When selecting a certain focal length f for the mirror, the object distance u and image distance v are approximately related through the formula $\frac{1}{f} = \frac{1}{u} + \frac{1}{v}$. In the previous chapter, we have determined the aberration coefficients in the case that $u = v = 2f$.

For different values of u the aberration coefficient change, since at a given angle, the electron will reach the mirror at a different distance from the optical axis and therefore sample a different part of the electrostatic potential of the mirror. Therefore it makes more

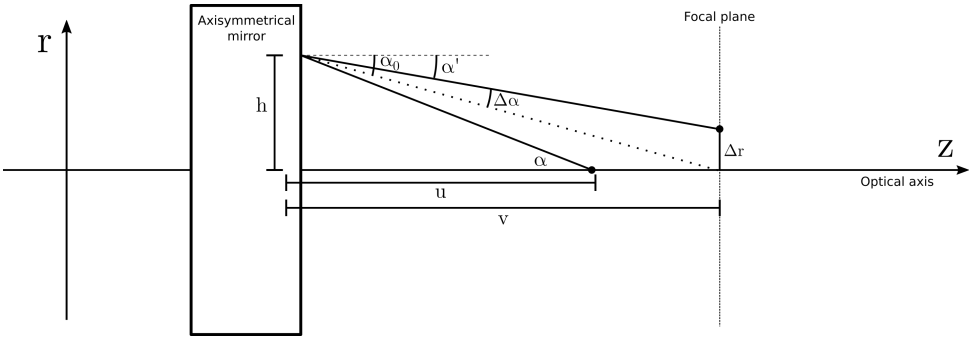

Figure 4.1: Definition of parameters that allow us to relate a_{ij} and C_{ij}. An angle after reflection of α_0 is needed to properly focus the electron in the focal plane. Because of aberrations a deviation of $\Delta\alpha$ in angle is present which results in a deviation of $\Delta r = \Delta\alpha v$ in the focal plane. Using this construction we can derive that $C_{ij} \propto u^i v$ as long as the mirror satisfies the thin lens approximation $\frac{1}{u} + \frac{1}{v} = \frac{1}{f}$.

sense to express the aberration coefficients in terms of the distance from the optical axis at which the electron reaches the mirror, which we call the height $h = \alpha u$ (see figure 4.1 and [39]).

Similarly, when changing the value of v, the aberration coefficients will change since Δr is dependent on v through the formula $\Delta r = \Delta\alpha v$. Here we use $\Delta\alpha = \alpha_0 - \alpha'$ as the deviation of the reflected angle α' from the needed angle α_0 to properly focus the electron. Our aberration coefficients will become independent from v if we define them using $\Delta\alpha$ instead of Δr.

Using h and $\Delta\alpha$ we now introduce our new aberration coefficients a_{ij} which are (by approximation) independent of u and v:

$$\Delta\alpha = \sum_{i,j=1(\text{i is odd})} a_{ij} h^i \left(\frac{\Delta E}{E}\right)^j \tag{4.1}$$

When we are properly in focus we have $a_{10} = 0$.

To find the relation between the aberration coefficients C_{ij} and the object and image distances u and v we find the relation between C_{ij} and a_{ij}. To do this, we consider that $\Delta r = \Delta\alpha v$ and $h = \alpha u$. Therefore every term in 4.1 contributes

$$\Delta r_{ij} = \underbrace{a_{ij} u^i v}_{C_{ij}} \alpha^i \left(\frac{\Delta E}{E}\right)^j$$

We have therefore derived that our aberration coefficients scale with u, v as

$$C_{ij} \propto u^i v \tag{4.2}$$

as long as the mirror satisfies the thin lens approximation $\frac{1}{f} = \frac{1}{u} + \frac{1}{v}$.

From this insight, we can transform the aberration coefficients found in the previous chapter to the aberration coefficients at any u and v using the following procedure.

Box 4.1.1. Computing aberration coefficients C_{ij} at $u \neq v$

1. Precompute the aberration coefficients as a function of lens voltage for a number of focal lengths ($u = v = 2f$)
2. Use interpolation to find the coefficients at the relevant electrode voltages and focal length
$$f = \frac{uv}{u + v}$$
3. Divide the coefficients to find the a_{ij} coefficients:
$$a_{ij} = \frac{C_{ij}}{u^i v} = \frac{C_{ij}}{(2f)^{i+1}}$$
4. Compute the relevant aberration coefficients as
$$C'_{ij} = a_{ij} u^i v$$

Equation 4.2 and the procedure in box 4.1.1 allow us to generalize the computations from the previous chapter to any values of u and v. This generalization allows us to predict what will be the effect on the aberration corrector when the distance between the mirrors (and therefore their focal lengths) is changed. However, when operating the DMC it's important to always keep the focus point of the mirrors and the lens preceding the corrector on the common cross over plane (CCP), and therefore to operate the mirrors with $u = v = 2f$. Keeping the crossovers in the CCP minimized the deflection aberrations imparted by the EBE deflector.

4.2 Aberrations of the double mirror combination

We now turn our attention to computing the aberrations of a combination of two electrostatic mirror, see figure 4.2. We use the convention that $M, M_\alpha > 0$ and $\alpha_2 < 0$. We can write the contributions of the aberration coefficients in the focal plane of the second mirror as

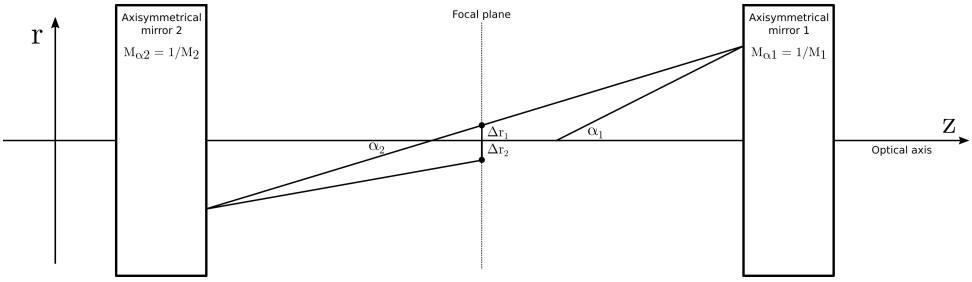

Figure 4.2: Diagram used for the derivation of equation 4.3. Notice that an underfocus (situation shown) now results in a negative $\Delta r_2 < 0$ value (instead of $\Delta r > 0$ in the single mirror case as shown in figure 4.1). In any case, the sign of the aberrations should always be chosen according to the convention shown in box 2.3.1.

$$\Delta r_{2,ij} = \left(-C_{2,ij}\alpha_2^i + M_2 C_{1,ij}\alpha_1^i\right)\left(\frac{\Delta E}{E}\right)^j$$

The relation between the angles is given by $\alpha_2 = -M_{\alpha 1}\alpha_1 = -\alpha_1/M_1$, therefore

$$\Delta r_{2,ij} = \left(\frac{C_{2,ij}}{M_1^i} + M_2 C_{1,ij}\right)\alpha_1^i\left(\frac{\Delta E}{E}\right)^j$$

Note that from equation 2.6 a minus sign should be added to the right-hand side when a spherical aberration is considered ($j = 0$). However, this has no effect on the end result, which is:

Box 4.2.1. DMC aberrations in terms of the single mirror aberrations

$$C_{ij} = \frac{C_{2,ij}}{M_1^i} + M_2 C_{1,ij} \quad (M_1, M_2 > 0) \tag{4.3}$$

The aberrations coefficients found using this formula are given in terms of α_1 and Δr_2. Just like in the single mirror case the aberration coefficients satisfy the sign convention given by box 2.3.1.

4.3 Requirements for aberration correction

The aberration coefficients are determined in terms of an angle and a focal plane. There is nothing preventing us from using the angle with the optical axis *at* the focal plane. This is actually the convention used for the objective lens since the aberration coefficients are usually given in terms of the deviation in the sample plane as a function of the angle at

the sample. The aberrations coefficients are then on the order of millimeters and usually scale linearly with the working distance.

It is also common when computing the aberration coefficients of the objective lens to assume the object point is in infinity, such that the beam is parallel to the optical axis before the objective lens. In this case, the aberration coefficients are written as $C_{ij}(\infty)$. To convert the aberration coefficients to their values at a certain magnification M_{obj} we can use

$$C_{ij}(M_{\text{obj}}) = (1 + M_{\text{obj}})^{i+1} C_{ij}(\infty)$$

(see [39] for a derivation).

To consider whether the aberrations of the objective lens have correctly been corrected, we have to transform the aberration coefficients of the objective lens and the aberration corrector to a common plane and angle. A natural choice is to use the focal plane of the second mirror (i.e. the first focal plane after the corrector) and the beam angles in this plane.

To transform the aberration coefficients of the objective lens to the focal plane of the second mirror, consider the beam path shown schematically in figure 4.3. The deviation in the focal plane of the second mirror $\Delta r'$ is related to the deviations in the sample plane by the magnification of the bottom einzel lens and the objective lens $\Delta r = M_{\text{BEL}} M_{\text{obj}} \Delta r'$. Similarly, the angles are related as $\alpha = \alpha'/(M_{\text{BEL}} M_{\text{obj}})$. Substituting these two formulas in equation 2.6 we can conclude that the aberration coefficients of the objective lens at the focal plane of the second mirror are

$$\frac{1}{\left(M_{\text{BEL}} M_{\text{obj}}\right)^{i+1}} C_{ij} = \left(\frac{1 + M_{\text{obj}}}{M_{\text{BEL}} M_{\text{obj}}}\right)^{i+1} C_{ij}(\infty) = \mu^{i+1} C_{ij}(\infty) \tag{4.4}$$

where we have introduced the variable

$$\mu = \frac{1 + M_{\text{obj}}}{M_{\text{BEL}} M_{\text{obj}}} \tag{4.5}$$

for convenience.

The aberration coefficients following from box 4.1.1 and equation 4.3 are already given in terms of the deviation in the focal plane of the second mirror. To express them in terms of the angle at this plane the coefficients need to be multiplied by $M_1^i M_2^i$. Let us write the result of this as C'_{ij}. The condition that the lowest order chromatic and spherical aberrations of the objective lens are corrected can now be expressed as:

$$C'_{11} = -\mu^2 C_{11}(\infty) \tag{4.6}$$

$$C'_{30} = -\mu^4 C_{30}(\infty) \tag{4.7}$$

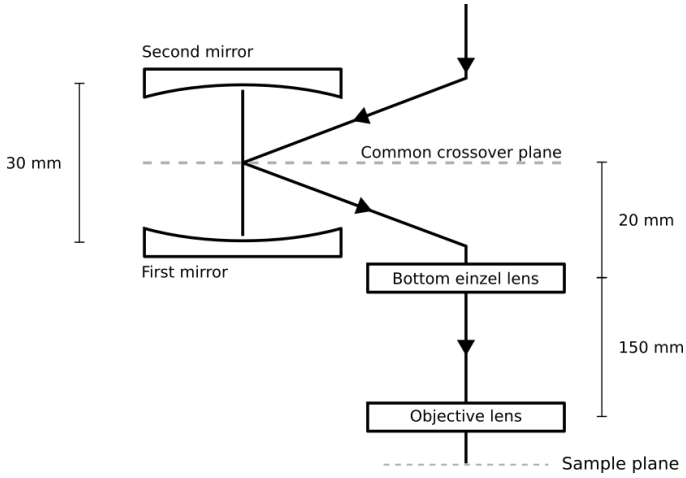

Figure 4.3: Beam path after the condenser lenses. A deflector deflects the beam towards the mirror axis. After a reflection from the bottom and top mirror, the beam is deflected back to the microscope axis. Here it is focused by the bottom einzel lens (BEL) and the objective lens before reaching the sample. The dashed line is called the common crossover plane (CCP) since the crossovers before and after the mirror reflections are in this plane. The real-world dimensions in the system are intellectual property. Therefore for this work we use the arbitrarily chosen dimensions shown in the figure.

4.4 Aberration matching procedure

While equations (4.6, 4.7) tell us the requirement that we need to fulfill in order to achieve aberration correction, it does not tell us how the DMC and the BEL magnification need to be configured. With the theory and numerical results produced until now, it would only be possible to use trial and error to try to satisfy equations (4.6, 4.7)

It turns out that we can derive from equations (4.6, 4.7) a so-called *matching condition* which will allow us to fulfill the two requirements exactly. To do this, consider that μ must have the same value in both equations and therefore

$$\frac{-C'_{11}}{C_{11}(\infty)} = \sqrt{\frac{-C'_{30}}{C_{30}(\infty)}} = \mu^2 \tag{4.8}$$

This is a relation between the spherical and chromatic aberration coefficients that is independent of μ. The key insight is to bring the coefficients related to the corrector to one side, and the coefficients related to the objective lens to the other side. This gives us our matching condition

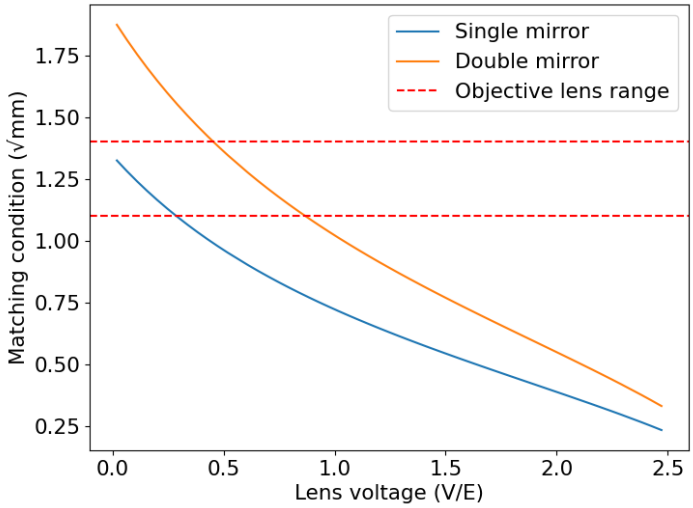

Figure 4.4: The left-hand side of the matching condition (equation 4.9) is plotted for the mirror shown in figure 3.1**a**. A distance of 15 mm is assumed between the mirror electrode and the common crossover plane. The aberrations used are plotted in figure 3.3 (focal length f = 7.5 mm). The difference between the single mirror and the double mirror values is exactly $1/\sqrt{2}$ if the mirror crossovers lie in the common crossover plane (unity magnification). This can be seen from equations 4.3 and 4.9. The aberrations of the objective lens are not given for reasons of intellectual property, but the range of expected values of $\frac{C_{11}}{\sqrt{C_{30}}}$ is given approximately to show that the DMC is capable of producing all necessary matching condition values.

Box 4.4.1. Aberration matching condition

$$\frac{-C'_{11}}{\sqrt{-C'_{30}}} = \frac{C_{11}(\infty)}{\sqrt{C_{30}(\infty)}} \tag{4.9}$$

Equation 4.9 is a necessary condition to fulfill the requirements (4.6, 4.7) that is independent of the magnification of the BEL and the objective lens. In other words, if the corrector fails the matching condition 4.9 the correction of both chromatic and spherical aberration can never be fulfilled simultaneously even when varying the BEL and objective lens magnifications.

The right-hand side of equation 4.9 is determined solely by the properties of the objective lens and is therefore considered to be a known quantity. By plotting the left hand side of equation 4.9 as a function of the electrode voltages applied to the electrostatic mirrors

an attempt can be made to find voltages that fulfill the matching condition. In figure 4.4 the left hand side of the matching condition (equation 4.9) has been plotted for the mirror currently integrated in the corrector (figure 3.1**a**) and an assumed distance between the mirror electrode and the CCP of 15 mm. It can be concluded that the corrector is capable of producing all the necessary matching condition values.

Once the matching condition has been fulfilled equation 4.8 can be used to find the optimal μ value. From the definition of μ (equation 4.5) we can see that this optimal μ value can be achieved by changing M_{BEL}. The most practical way to do this is to change the image length v_{BEL} because changing u_{BEL} would shift the focal plane of the second mirror and thereby change the carefully chosen aberrations of the corrector.

We can solve for the value of v_{BEL} analytically. If d_{BO} is the distance between the BEL and the objective lens we know

$$M_{\mathrm{BEL}} = \frac{v_{\mathrm{BEL}}}{u_{\mathrm{BEL}}} \qquad M_{\mathrm{obj}} = \frac{\mathrm{WD}}{d_{\mathrm{BO}} - v_{\mathrm{BEL}}}$$

where WD is the distance between the objective lens and the sample (the working distance). Substituting these values in the definition of μ and solving for v_{BEL} we find

$$v_{\mathrm{BEL}} = \frac{(d_{\mathrm{BO}} + \mathrm{WD})u_{\mathrm{BEL}}}{\mathrm{WD}\mu + u_{\mathrm{BEL}}} \tag{4.10}$$

Fulfilling the matching condition and choosing the correct v_{BEL} is sufficient to satisfy equations (4.6, 4.7). The procedure for achieving the correction of the lowest order chromatic and spherical aberrations has been summarized in box 4.4.2. In tables 4.1 and 4.2 this procedure has been followed to achieve simultaneous correction of the chromatic and spherical aberrations for the system shown in figure 4.3.

Box 4.4.2. Procedure for correcting lowest order chromatic and spherical aberrations

1. Compute the right-hand side of the matching condition using the aberration coefficients of the objective lens

$$\frac{C_{11}(\infty)}{\sqrt{C_{30}(\infty)}}$$

2. From the previously computed aberration coefficients at the relevant focal length, compute the matching condition values that can be produced by the DMC. If the crossovers lie in the CCP, the DMC aberrations will simply be double the single mirror aberrations (equation 4.3). If the crossovers do not lie in the CCP, use box 4.1.1 and equation 4.3 to find the aberration coefficients. Use interpolation to find the mirror voltages that satisfy the matching condition exactly

$$\frac{-C'_{11}}{\sqrt{-C'_{30}}} = \frac{C_{11}(\infty)}{\sqrt{C_{30}(\infty)}}$$

3. Compute the optimal μ value using

$$\mu^2 = \frac{-C'_{11}}{C_{11}(\infty)} = \sqrt{\frac{-C'_{30}}{C_{30}(\infty)}}$$

4. This optimal μ value can be achieved by changing v_{BEL} to

$$v_{\mathrm{BEL}} = \frac{(d_{\mathrm{BO}} + \mathrm{WD})u_{\mathrm{BEL}}}{\mathrm{WD}\mu + u_{\mathrm{BEL}}}$$

C_c obj (mm)	C_s obj (mm)	$C_c/\sqrt{C_s}$	Lens volt. (V/E)	Mirror volt. (V/E)	C_c (mm)	C_s (mm)	μ
0.5	0.5	0.707	1.64	-1.40	-898	-3.23e+06	59.94
0.5	1.0	0.500	2.11	-1.51	-430	-1.48e+06	41.49
1.0	0.5	1.414	0.438	-1.19	-3825	-1.46e+07	87.47
1.0	1.0	1.000	1.04	-1.28	-1919	-7.37e+06	61.96
1.0	1.5	0.816	1.40	-1.35	-1234	-4.57e+06	49.67
1.5	1.0	1.500	0.346	-1.17	-4245	-1.60e+07	75.23
1.5	1.5	1.225	0.679	-1.22	-2914	-1.13e+07	62.34
1.5	2.0	1.061	0.934	-1.26	-2174	-8.40e+06	53.84
2.0	1.5	1.633	0.214	-1.15	-4890	-1.79e+07	69.93
2.0	2.0	1.414	0.438	-1.19	-3825	-1.46e+07	61.85

Table 4.1: For a given objective lens (obj) aberrations the procedure shown in box 4.4.2 is followed to achieve complete cancellations of the lowest order chromatic and spherical aberrations. The mirror geometry used is shown in figure 3.1**a**. The object and image distance of the mirrors is chosen as 15 mm as shown in figure 4.3. The mirror aberrations are for a single mirror and are plotted in figure 3.3 (f = 7.5 mm). The aberrations in the CCP for both mirrors are simply double the aberrations shown since M = 1 for both mirrors (equation 4.3). How to achieve the correct μ value for different objective lens working distances is shown in table 4.2.

μ	WD (mm)	v_{BEL} (mm)	M_{BEL}	M_{obj}
59.94	2	21.73	1.087	0.0156
59.94	3	15.31	0.768	0.0223
41.49	2	29.52	1.476	0.0166
41.49	3	21.18	1.059	0.0233
87.47	2	15.59	0.780	0.0149
87.47	3	10.84	0.542	0.0216
61.96	2	21.12	1.056	0.0155
61.96	3	14.86	0.743	0.0222
49.67	2	25.47	1.274	0.0161
49.67	3	18.11	0.905	0.0228
75.23	2	17.83	0.892	0.0151
75.23	3	12.45	0.623	0.0218
62.34	2	21.01	1.051	0.0155
62.34	3	14.78	0.739	0.0222
53.84	2	23.81	1.191	0.0159
53.84	3	16.86	0.843	0.0225
69.93	2	19.02	0.951	0.0153
69.93	3	13.32	0.666	0.0220
61.85	2	21.16	1.058	0.0155
61.85	3	14.89	0.744	0.0222

Table 4.2: Equation 4.10 is used to find the v_{BEL} needed to achieve the required μ value (equation 4.5). The μ values are taken from table 4.1. The procedure works for any objective lens working distances (WD) but here it is chosen as 2 mm or 3 mm. The relevant magnifications are computed using the arbitrarily chosen column dimensions shown in figure 4.3.

5

Mirror design optimization

In chapter 4 we studied how the aberration corrector can be used effectively to optimize the resolution of the scanning electron microscope. The current design of the aberration corrector makes use of the mirror design elaborated in chapter 3 which was based on the design presented by H. Dohi and P. Kruit (see [7]). In this chapter, we will consider evaluation criteria that we can use to determine the quality of a mirror design. We study the effect of changing certain geometrical parameters on these evaluation criteria. This knowledge can be used in a future mirror design to achieve a mirror of higher quality.

5.1 Mirror evaluation criteria

In this section, we motivative the evaluation criteria summarized in table 5.1. The symbols and the terminology used in the table are explained in the following subsections.

To compute the numerical values associated with the evaluation criteria we need to decide which voltages to apply to the mirror electrodes. In chapter 4 we learned that the value of the aberration matching condition (equation 4.9) is paramount in achieving correction of both the spherical and chromatic aberrations of the objective lens. It is therefore reasonable to calculate the evaluation criteria at mirror electrode voltages for which the corresponding aberrations fulfill the same matching condition. The value of the matching condition depends on the aberrations of the objective lens and therefore on experimental parameters like the working distance. To limit the complexity of the calculations we arbitrarily assume that the objective lens aberrations are

$$C_{c,\mathrm{obj}} = C_{s,\mathrm{obj}} = 1.5\,\mathrm{mm} \tag{5.1}$$

The total corrector aberrations will be twice the single mirror aberrations when both mirrors are excited with equal voltages and their focus points lie correctly in the common

crossover plane (equation 4.3 with $M_1 = M_2 = 1$). Therefore to fulfill the matching condition we need

$$\frac{-2C_c}{\sqrt{-2C_s}} = \frac{1.5}{\sqrt{1.5}} \quad \Longrightarrow \quad \frac{-C_c}{\sqrt{-C_s}} = \sqrt{\frac{1.5}{2}} \approx 0.866 \sqrt{\text{mm}} \tag{5.2}$$

for our single mirror aberrations C_c, C_s. For the triode designs this chosen value of the matching condition uniquely determines the voltages that need to be applied to the electrodes. For every mirror design considered an aberration curve as is shown in figure 3.3 is computed after which a cubic spline interpolation is used to find the mirror voltages that fulfill the matching condition 5.2. The distance between the common crossover plane (CCP) and the mirror electrode is assumed to be 15 mm (figure 4.3). Now that we have clarified for which mirror electrode voltages the comparisons will be made, we will now elaborate on the evaluation criteria listed in table 5.1.

Allowed beam energy

The geometry of the mirror determines the maximum beam energy that can be used with the mirror. The voltages that need to be applied to the mirror electrodes scale linearly with the beam energy used. However, as the voltages applied to the electrodes increase a large potential gradient will arise between the positive lens electrode and the negative mirror electrode. This can induce a spontaneous current path through the spacer separating the electrodes, potentially damaging the electrostatic mirror. As a rule of thumb, these breakdown events occur at gradients of more than $5\,\text{keV}\,\text{mm}^{-1}$. We can therefore estimate the maximum allowed beam energy by considering when the gradient between the lens and mirror electrode surpasses this value.

Sensitivity to misalignment

The operation of the aberration corrector depends on a correct beam delivery from the top deflector and the top einzel lens. These elements are responsible for focusing the electron beam on the CCP between the two electrostatic mirrors. In practice, perfect beam delivery is never achieved. Factors like machining tolerance and misalignment of the elements above the corrector will result in the crossover point being not exactly in the CCP and not laterally centered with respect to the mirrors. In theory, the excitation of the top einzel lens and top deflector can be adjusted to achieve near-perfect beam delivery, but in practice, the lack of feedback on the exact position of the crossover with respect to the CCP makes this unachievable.

The voltages found using the method explained in chapter 2 ensure that a beam that is focused in the CCP is reflected to the same focus position. This means that we operate the mirror using a $M = -1$ magnification (a $M = 1$ mode is also possible but not considered here). If the beam is delivered laterally displaced by an amount r in the CCP the aberration corrector could still work adequately since after reflecting from both mirrors the beam is

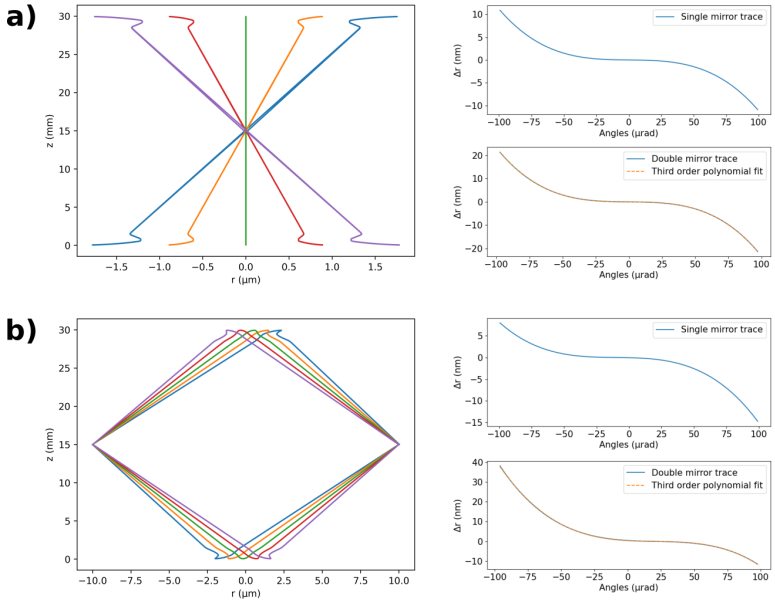

Figure 5.1: **a)** Electron traces for a double reflection in case of no displacement. The intersection in the focal plane Δr with respect to the central ray is calculated and plotted after reflection of the first mirror (single mirror trace) and after reflection of both mirrors (double mirror trace). The spherical aberration of the mirrors causes the deviation Δr to be a third-order function of the ray angle. As predicted by equation 4.3 the deviation in the focal plane after reflection off both mirrors is double the deviation after reflection of only the first mirror. **b)** Electron traces for a double reflection in the case of a displacement of 10 µm. The beam is deflected in the common crossover plane (midplane) twice to ensure the central ray hits the mirror centrally in both reflections. After two reflections the deviation Δr is not a third-order function of the ray angle but instead given by a more general third-order polynomial. The second-order coefficient C_{20} which contributes to the deviation as $C_{20}\alpha^2$ cannot be neglected anymore.

focused back at the same spot where it was delivered (i.e. with the same displacement). The EBE unit has enough degrees of freedom to ensure the electron beam hits the bottom mirror and top mirror centrally. In this condition the EBE unit would still be capable of correctly inserting the beam back into the microscope axis, albeit with a lateral displacement on the same order as r. Unfortunately, it is found numerically that a round trip through the corrector with a beam that is initially displaced in the CCP leads to a C_{20} aberration, see figure 5.1. The more the beam is initially displaced the larger the C_{20} value will be. Possible C_{00} and C_{10} contributions are not problematic since they can be compensated by a deflection or a defocus respectively. Since a (perfectly) axisymmetric objective lens has no compensating C_{20} contribution we expect the C_{20} term resulting from the misalignment

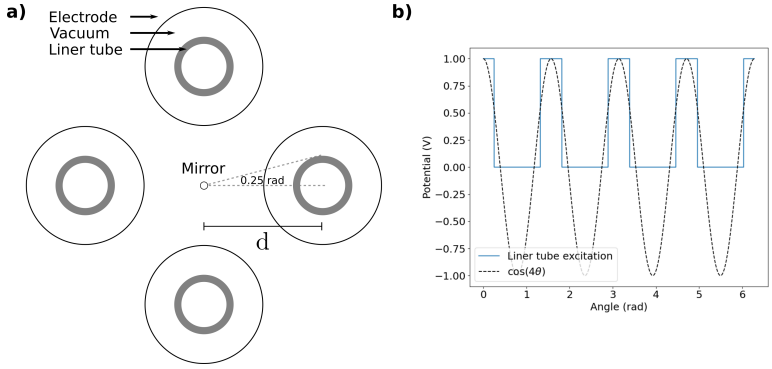

Figure 5.2: **a)** The liner tubes shielding the electrons at the mirror axis from electrostatic interference from the microscope axis are placed in an octupole configuration to minimize deflection fields (see [28]). The microscope axis protrudes through the center of one of the liner tubes. The exact dimensions are not shown since this is considered sensitive information. The distance between the mirror axis and the center of the liner tube is denoted by d. **b)** The first non-zero multipole field of the liner tubes is an octupole ($n = 4$). Fourier analysis can be used to find the corresponding octupole coefficient (equation 5.3). The coefficient is calculated to be $c_4 \approx 0.54\,\mathrm{V/mm}^4$

to result in a loss of resolution. We therefore quantify the sensitivity to misalignment by the C_{20} coefficient after two reflections at a misalignment of 10 µm. The smaller the C_{20} coefficient is, the less sensitive the corrector will be to misalignment.

Electrostatic interference from the grounded liner tubes

To shield the electrons traveling along the microscope axis from the electrostatic fields present on the mirror axis we make use of *liner tubes*. These are small grounded hollow cylinders concentric with the microscope axis. Since these liner tubes are grounded they affect the electrostatic force felt by the electrons at the mirror axis. In an attempt to attenuate the deflection fields created by the liner tubes they are placed around the mirror axis in an octupole configuration, see figure 5.2 and [28].

To study the electrostatic interference realistically and accurately a 3D simulation needs to be performed. Considering that tracing electrons in commercial 3D software packages is computationally costly and the fact that many thousands of electrons need to be traced to study all the mirror designs presented here we see that an exact computation is infeasible at this point. To still quantify the effect of the liner tubes we consider the liner tubes as an octupole perturbation and take into account the resulting force while tracing the electrons (see also appendix C in [28]). The percentual difference of the spherical aberration coefficients with and without the octupole perturbation is a measure of the impact of the liner tubes.

Let us now consider the exact electrostatic force added to the tracing routine. We make the simplification that the liner tube configuration results in a pure octupole field, and is therefore of the form (see equation 5.1 of [39]):

$$\Phi_4 = c_4 r^4 \cos(4\phi)$$

Strictly speaking, a $\sin(4\phi)$ term would also be present, but we can choose our coordinate system such that the liner tube potential is an even function of ϕ and therefore the $\sin(4\phi)$ term vanishes. We can find the c_4 coefficient by using Fourier analysis:

$$c_4 r^4 = \frac{1}{\pi} \int_0^{2\pi} V(\phi) \cos(4\phi) d\phi \tag{5.3}$$

We take the integral through the center of the liner tubes, which implies $r = d$, where d is the distance between the mirror axis and the center of the liner tubes (see figure 5.2**a**). If we take $V(\phi)$ to be unity on the liner tubes and zero everywhere outside the liner tubes we can compute (see figure 5.2**b**):

$$c_4 \approx 0.54\,\mathrm{V/mm^4}$$

In reality, the liner tubes are grounded and therefore the unity excitation is unrealistic. To find the true excitation we make an argument based on superposition. We know that in the center of the grounded liner tubes the potential must be zero. In our axisymmetrical model, the potential at this location is determined by the geometry of the mirrors and the excitation of their electrodes. Let us write $V_\mathrm{m}(z) = V_\mathrm{mirror}(r = d, z)$ for the potential that follows from the boundary element method at the center of one of the liner tubes. If the potential needs to be zero at this location, by superposition the excitation of the liner tubes needs to be $-V_\mathrm{m}(z)$. Therefore

$$-V_m(z)\Phi_4 = -V_\mathrm{m}(z) c_4 r^4 \cos(4\phi)$$

is the perturbation we will use in the tracing routine. To keep our tracing two dimensional we choose ϕ such that $E_\phi = -\frac{\partial \Phi_4}{\partial \phi} \propto \sin(4\phi)$ is zero. The corresponding electric force is then

$$E_r = -\frac{\partial \Phi_4}{\partial r} = \pm 4 V_\mathrm{m}(z) c_4 r^3$$

where the sign is determined by the value of $\cos(4\phi)$, or in other words, by the orientation of the electron trajectory with respect to the liner tubes. For both choices of sign, we can compute a spherical aberration coefficient which we will denote as C_s^+ and C_s^-. The quantity

$$\left| \frac{C_s^+ - C_s^-}{C_s} \right|$$

is the spread in spherical aberration that we expect as a result of the liner tube perturbation, where C_s is the unperturbed spherical aberration.

Criteria	Quantification	Objective
Allowed beam energy	E_{beam} Maximum beam energy for which the corresponding mirror voltages will not lead to flashover in the mirror.	Higher is better
Sensitivity to misalignment	C_{20} Parasitic C_{20} aberration after two reflections starting from a 10 µm misalignment	Lower is better
Electrostatic interference from the grounded liner tubes	$\lvert\Delta C_{30}/C_{30}\rvert$ Spread in spherical aberration of the reflected beam caused by the octupole perturbation.	Lower is better

Table 5.1: Evaluation criteria used to judge the quality of an electrostatic mirror. The symbols and the terminology are elaborated in detail in section 5.1.

5.2 Proposed mirror designs

As a first practical improvement over the current design (figure 3.1) we change the thickness of all electrodes used in the mirror to [redacted] µm. This thickness is a suggestion by the technical support in charge of fabricating this mirror and is a tradeoff between the time needed to etch through the wafer and the fragility of the resulting electrodes. To elucidate further improvements, the impact of changing four geometrical parameters on the evaluation criteria is studied. These geometrical parameters are shown in figure 5.3 and chosen because they are believed to have the largest effect on the evaluation criteria. The parameters chosen are the distance between the ground and the lens electrode, the distance between the lens and the mirror electrode, the radius of the aperture in the lens electrode and the radius of the aperture in the mirror electrode. In section 5.5 we elaborate on a tetrode mirror design (also shown in figure 5.3) and study how the evaluation criteria change with the voltage applied on the auxiliary electrode.

5.3 Effects of changing the geometrical parameters

The effect of varying the four chosen geometrical parameters is shown in figure 5.4. The values on the horizontal axis represent the geometrical parameters normalized to the val-

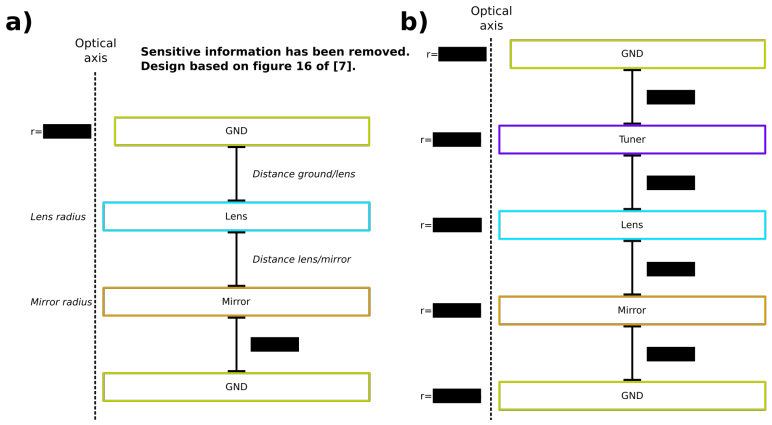

Figure 5.3: **a)** The previous mirror design shown in figure 3.1 is adapted from the design by H. Dohi and P. Kruit [7] by changing all the electrode thicknesses to [redacted] µm as motivated in the text. In this geometry four geometrical parameters are varied and the results are studied according to the evaluation criteria of section 5.1. The parameters to be varied are the distance between the ground and the lens electrode, the distance between the lens and the mirror electrode, the aperture radius in the lens electrode, and the aperture radius in the mirror electrode. The parameters are shown in italic. The values of these parameters in the current mirror design are shown in table 5.2. The effect of changing these geometrical parameters is shown in figure 5.4. **b)** The current triode mirror design is extended with a 'tuner' electrode between the ground and lens electrode to form a tetrode mirror design. This design is studied in section 5.5.

ues in the current design which are shown in table 5.2. An extra distance of [redacted] µm is added to the distance between the electrodes to account for the glue layers but is ignored when calculating the normalized value (so a normalized value of 2 corresponds to 2 × 500+ [redacted] = [redacted] µm).

From figure 5.4 it is clear that the most critical design parameters are the radius of the aperture in the mirror electrode, and the distance between the lens and mirror electrode. In contrast, the radius of the aperture in the lens electrode, and the distance between the lens electrode and the ground electrode have only a small effect on the evaluation criteria.

Furthermore, it is also evident from the plotted mirror electrode voltage in figure 5.4 that increasing the mirror radius necessitates increasing the magnitude of the mirror electrode voltage. This can be understood physically since the larger mirror electrode excitation compensates for the increase in the mirror electrode radius in such a way that the electrons still encounter a properly curved electrostatic field. The corresponding effect for the lens electrode is also present but less pronounced, implying that the focusing effect of the lens electrode is not significantly degraded by a bigger aperture in the lens electrode.

The C_{20} contribution resulting from misalignment seems to be affected significantly only

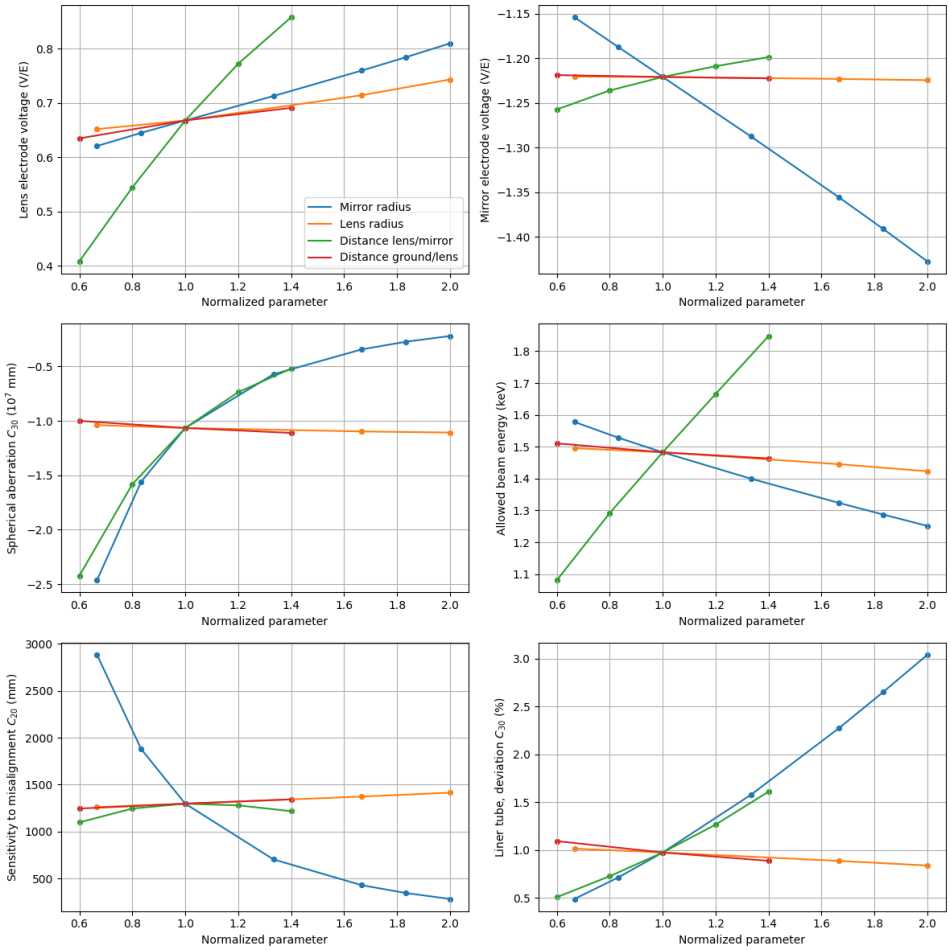

Figure 5.4: The evaluation criteria are plotted as a function of the geometrical parameters shown in figure 5.3. Which geometrical parameter is varied is shown in color, while the value of the geometrical parameter is shown on the horizontal axis normalized to the value in the current design (table 5.2). When one parameter is varied, the value of other parameters is kept fixed at the value in the current design. It can be seen that the aperture radius in the mirror electrode and the distance between the lens and mirror electrode have a larger effect on the evaluation criteria than the aperture radius in the lens electrode and the distance between the lens and ground electrode. The chromatic aberration coefficient can be computed from the spherical aberration coefficient using the matching condition (equation 5.2).

	Current design (μm)	Optimized design (μm)
Mirror radius	75	[redacted]
Lens radius	75	75
Distance lens/mirror	500 (+[redacted])	[redacted] (+[redacted])
Distance ground/lens	500 (+[redacted])	500 (+[redacted])

Table 5.2: Values of the geometrical parameters (shown in figure 5.3) for the mirror design currently in the corrector as designed by H. Dohi and P. Kruit [7]. [redacted] μm is added to the distance between the electrodes to account for two glue layers. In section 5.4 we substantiate the choice for the new values of the geometrical parameters. The result on the evaluation criteria for the optimized mirror design is shown in table 5.4.

by the aperture in the mirror electrode. When varying the aperture radius in the mirror electrode the C_{20} curve resembles qualitatively the (absolute value of the) C_{30} curve. Interestingly, a larger distance between the lens and mirror electrode reduces the C_{30} coefficient while not appreciably affecting the C_{20} value. The reduction in the C_{30} aberration can be explained by the fact that the electrons will reach the mirror electrode closer to the optical axis when focussed by the lens electrode. As argued in section 3.3 this reduces the aberrations of the mirror. Apparently, a similar reasoning for the C_{20} coefficent does not apply.

Finally, from figure 5.4 it can be seen that the liner tubes cause a 1% deviation in the C_{30} value, as computed using the octupole perturbation method explained in the previous section. The C_{30} deviation increases rapidly with the radius of the mirror electrode and the distance between the lens and mirror electrode.

5.4 Local optimization of the geometrical parameters

Now that we have calculated what the effects are of changing the geometrical parameters we can attempt to improve the mirror design. We first discuss what are the acceptable values for the evaluation criteria, after which we can use figure 5.4 as guidance on how the geometry of the mirror should be changed. Given that the size of the lens electrode aperture and the distance between the lens and ground electrode have little effect we need not modify them. Increasing the mirror aperture radius degrades the allowed beam energy and the liner tube deviation, while it improves the tolerance to misalignment. The distance between the lens and mirror electrode improves the allowed beam energy, degrades the liner tube deviation, and has little effect on the sensitivity to misalignment.

We estimate the allowed values for the liner tube deviation and the sensitivity to misalignment. For the liner tube deviation, we consider that the FW50 probe size d at the sample

plane as a result of a residual uncorrected C_s is given by[40]:

$$d_{30} = 0.18 C_s \alpha^3 \tag{5.4}$$

Let us assume that we aim for a resolution improvement of a factor κ over the non aberration corrected case. If the probe size as a result of diffraction is roughly as big as the probe size resulting from spherical aberration, we need to improve both by the factor κ. The improvement in the probe size resulting from diffraction effects can be achieved by increasing the beam semi-angle α with the factor κ. The decrease in spherical aberration needs to be achieved by a suitable correction of C_{30}. If we use a prime for the values in the aberration corrected case we have:

$$d'_{30} = \frac{1}{\kappa} d_{30} \quad \Longrightarrow \quad 0.18 C'_s (\kappa\alpha)^3 = \frac{0.18}{\kappa} C_s \alpha^3 \quad \Longrightarrow \quad C'_s = \frac{1}{\kappa^4} C_s$$

So a resolution improvement of a factor κ in the aberration corrected case can be achieved by decreasing the spherical aberration by a factor $\frac{1}{\kappa^4}$. Let us assume here that we aim for a resolution improvement of $\kappa = 2.5$ to make the corrector commercially viable. This means we need to correct the spherical aberration coefficient by 97.5% and therefore can tolerate a maximum spread in the spherical aberration of 2.5%. To allow some margin of error we allow a spread of the spherical aberration by the liner tubes of 2%.

Getting a substantiated bound on the C_{20} value needs a more elaborate argument. We expect for the probe size of the C_{20} contribution a formula similar to 5.4, although with a coefficient that might differ from 0.18. A quick computation assuming a uniform angular distribution of the electrons shows this coefficient to be close to 1 in the focal plane. Even though the probe size might be smaller when a small defocus is applied we assume the following for an upper bound on the C_{20} probe size:

$$d_{20} = C_{20} \alpha^2 \tag{5.5}$$

To limit the loss of resolution by misalignment we make the arbitrary but reasonable requirement that $d_{20} < 0.5\,\text{nm}$ at the sample plane. At our assumed aberrations (equation 5.1) the optimal beam semi-angle at the sample plane is close to 10 mrad. If we again assume a correction factor of $\kappa = 2.5$ we need the microscope to operate at a beam semi-angle of 25 mrad. In this case from $d_{20} < 0.5\,\text{nm}$ and equation 5.5 we have the requirement $C_{20} < 800\,\text{nm}$ at the sample plane. Using formula 4.4 we translate this value back to the CCP to find $C'_{20} = \mu^3 C_{20}$. The value of μ at our assumed aberrations (equation 5.1) can be read from table 4.1 to be $\mu = 62.43$, therefore $C'_{20} \approx 200\,\text{mm}$ is the upper bound for the tolerable C_{20} value. The values for C_{20} shown in figure 5.4 are calculated at a misalignment of 10 µm. Given that we expect to be able to tweak the deflection at the top deflector to an accuracy of 0.1 mrad we expect the lateral displacement to be about ~ 2 µm, or a factor of 5 lower than used in figure 5.4. To account of this we increase our C_{20} bound by the same factor to conclude that we need $C_{20} < 1000\,\text{mm}$ at a misalignment of 10 µm. Here we have used the fact that C_{20} grows linearly with the lateral displacement (misalignment) off the crossover. We know this since it can be checked trivially numerically, and furthermore, the

	Current design	**Optimized design**
Lens voltage	0.668 V/E	0.886 V/E
Mirror voltage	-1.22 V/E	-1.21 V/E
Spherical aberration C_s	-1.07×10^7 mm	-0.389×10^7 mm
Allowed beam energy	1.5 keV	1.9 keV
Sensitivity to misalignment C_{20}	1.3×10^3 mm	1.0×10^3 mm
Spread in spherical aberration	0.98 %	2.0 %

Table 5.3: For the mirror design currently in the corrector and the optimized design (see figure 5.3 and table 5.2) we show the voltages at the matching condition (equation 5.2). Using these voltages, the spherical aberration C_s and the three evaluation criteria discussed in the main text are computed. The chromatic aberration coefficient C_c follows from the spherical aberration coefficient C_s and the assumed matching condition 5.2. The optimized design allows for a higher beam energy and is less sensitive to misalignment. As a tradeoff the spread in spherical aberration caused by the liner tubes is accepted to be 2.0%.

C_{20} aberration is closely related to the well known coma aberration, which grows linearly with the displacement.

From the previous paragraphs, we concluded that we should optimize the radius of the mirror aperture and the distance between the lens and mirror electrode while limiting the C_{30} spread caused by the liner tubes to 2% and limiting the C_{20} coefficient to 1000 mm in the CCP. Considering figure 5.4 we see that we need to increase the radius of the mirror aperture to fulfill the condition on the C_{20} value. At the same time, it would be beneficial to increase the distance between the lens and mirror electrode until reaching the 2% bound on the C_{30} spread to maximize the allowed beam energy. In other words, if we tweak the geometrical parameters to achieve the mentioned bounds on C_{20} and the C_{30} spread we maximize the allowed beam energy. In fact, we can use the first derivatives of the curves in figure 5.4 to build up a small 2×2 linear problem in which we can solve for the values of our geometrical parameters. The resulting radius of the mirror aperture is found to be [redacted] µm and the spacing between the lens and mirror electrode [redacted] µm (already including the glue layers). A calculation reveals that these parameters do not reproduce our required C_{30} spread of 2% and C_{20} value of 1000 mm. The reason for this is that the assumed linearity of the problem and the independentness of the two geometrical parameters is not realistic. Fortunately, starting from the new values of our geometrical parameters we can produce a figure similar to 5.4 and build up a new linear system, which reveals the needed geometrical parameters to be [redacted] µm for the radius of the mirror aperture and [redacted] µm for the spacing between the lens and mirror electrode (already including the glue layers). As shown in table 5.4 these values for the geometrical parameters do reproduce the correct values for the sensitivity to misalignment and the spread in the spherical aberration. The maximum allowed beam energy is increased to 1.9 keV.

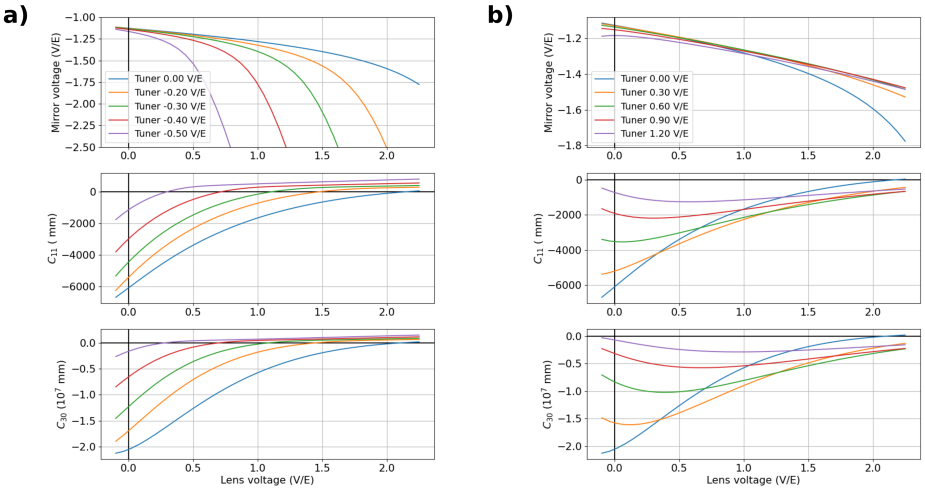

Figure 5.5: Aberration curves of the tetrode mirror shown in figure 5.3 for different voltages applied to the tuner electrode. As motivated in the text the mirror aberrations decrease as the tuner voltage is increased. The distance from the focus points to the mirror is taken to be 15 mm (see figure 4.3). **a)** Aberration curves for negative tuner voltages. **b)** Aberration curves for positive tuner voltages. The aberration curves for a grounded tuner electrode are shown in both plots (in blue) as a reference.

5.5 Tetrode mirror

Having studied a number of triode mirror designs, we now apply the evaluation criteria to a tetrode design. This allows us to study whether the auxiliary degree of freedom presented by an extra electrode has a large effect on the evaluation criteria. The tetrode mirror studied in this section is shown in figure 5.3. The mirror is constructed by taking the current mirror design (figure 5.3 and table 5.2) and adding an electrode between the lens and ground electrode. For lack of a better name, we call this electrode the 'tuner' electrode since its goal is to make the properties of the mirror tunable. It can be held at a fixed voltage in an experimental setting since the focusing behavior of the mirror can already be controlled using the lens and mirror electrodes. We choose the tuner electrode to be identical in geometry to the lens electrode.

The computed spherical and chromatic aberrations as a function of the electrode voltages are shown in figure 5.5. Both the spherical and chromatic aberrations are reduced when the tuner electrode voltage is large. As argued in chapter 3 the mirror aberrations are smaller when the electrons are focused close to the optical axis when reflecting off the mirror electrode. Since the tuner electrode causes a stronger focusing effect the reduction

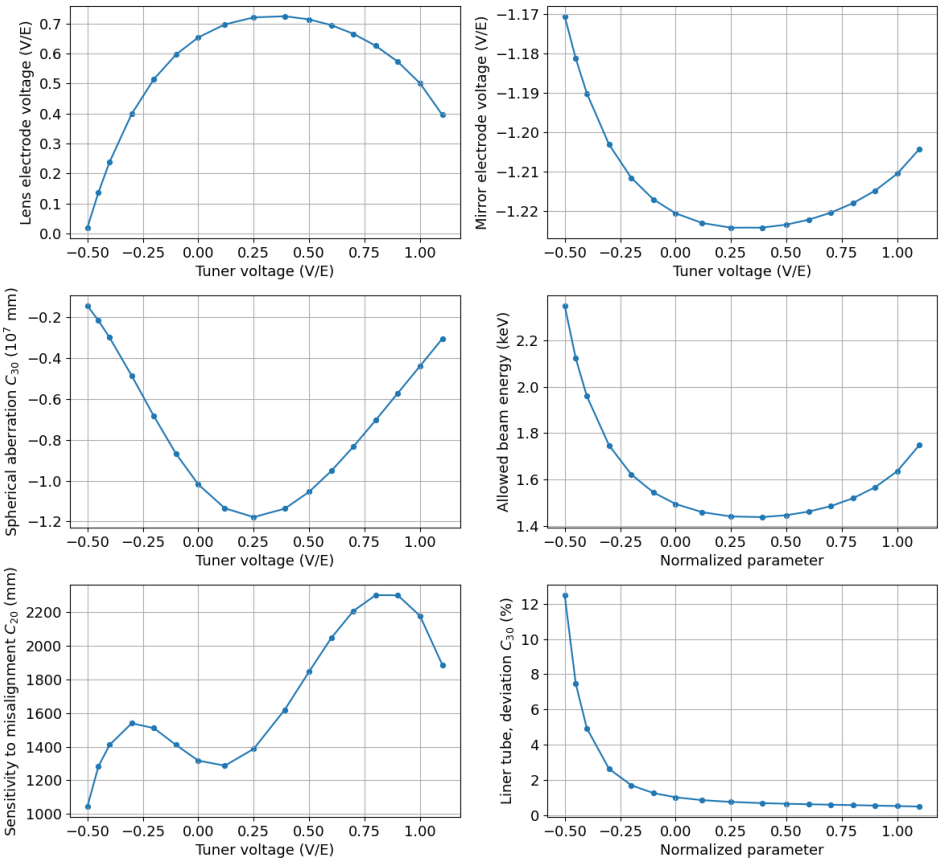

Figure 5.6: The evaluation criteria are computed for the tetrode mirror (figure 5.3). The electrode voltages are chosen such that the aberrations of the mirror (figure 5.5) fulfill the matching condition (equation 5.2), this makes the comparison with figure 5.4 straightforward. It can be seen that the magnitudes of the mirror aberrations decrease rapidly when the voltage on the tuner electrode is increased in absolute value. The chromatic aberration coefficient can be computed from the spherical aberration coefficient using the matching condition (equation 5.2).

in aberrations is expected.

To make a comparison with the triode mirror designs easy, we compute the evaluation criteria under the same condition as used for the triode mirrors. This means that we assume the distance between the mirror and the CCP to be 15 mm and that we pick the voltages of the tetrode mirror such that it fulfills the matching condition chosen previously (equation 5.2). The result can be seen in figure 5.6. The different tuner voltages are shown on the horizontal axis. Again it can be seen that a large tuner voltage (either negative or positive) reduces the C_{30} aberration of the mirror. Furthermore, the tuner voltage has a large impact on the lens electrode voltage needed to achieve correct focusing. The impact on the mirror electrode voltage is much smaller in comparison. The maximum allowed beam energy is closely related to the voltage gradient between the lens and mirror electrode and since the mirror electrode voltage changes only marginally, the maximum allowed beam energy follows a trend that is 'inverted' with respect to the lens electrode voltage. The sensitivity to misaligment has a very non-linear dependence on the tuner voltage, but the trend is a larger sensitivity to misalignment with an increasing tuner voltage. Finally, the liner tube deviation seems to increase substantially when a negative voltage is applied to the tuner electrode, whereas a positive tuner electrode voltage seems to decrease the liner tube impact compared to the triode designs.

5.6 Conclusion

We introduced relevant evaluation criteria for the electrostatic mirrors, which are the maximum allowed beam energy, the sensitivity of the mirror to misalignment, and the influence of the octupole perturbation caused by the grounded liner tubes. Possible approaches to quantify these criteria were presented in detail. For the maximum allowed beam energies the voltage gradients present while fulfilling matching condition 5.2 were compared to gradients at which flashover events are expected. The sensitivity to misalignment was found to be determined by a C_{20} contribution which arises when the beam is initially displaced in the CCP. Finally, for the interference from the grounded liner tubes an octupole perturbation was added to the electron tracing routine to estimate its impact.

For the triode designs, the most critical geometrical parameters were found to be the distance between the lens and mirror electrode and the aperture radius of the mirror electrode (figure 5.4). The aperture radius of the lens electrode and the distance between the ground and lens electrode seem to have a small effect on the properties of the mirror. The spread in spherical aberration caused by the grounded liner tubes increases with the distance between the lens and mirror electrode and also with the aperture radius of the mirror electrode. The triode mirror design also seems to become less sensitive to misalignment if the aperture radius of the mirror electrode is increased. Based on these insights a new mirror design is proposed, in which the mirror aperture radius is increased to [redacted] µm while the distance between the lens and mirror electrodes is increased to [redacted] µm (table 5.2). The new mirror improves upon the sensitivity to misalignment and the allowed beam energy but as a tradeoff suffers from a larger C_s spread from the liner tubes (table 5.4).

The same evaluation criteria under the same mirror operating conditions were applied to a proposed tetrode design, which was constructed by adding an electrode to the current triode mirror design (figure 5.3). The voltages applied to this 'tuner' electrode have a large effect on the properties of the mirror (figure 5.6). A large positive tuner voltage seems to decrease the magnitude of the mirror aberrations, increase the maximum allowed beam energy, increase the sensitivity to misalignment and decrease the impact of the grounded liner tubes.

6

Experimental progress

During the writing of this thesis, the SU8030 microscope in which the corrector was placed was in repair for a considerable amount of time. Still, after the repair, enough experimental time was available to make important observations about the state of the system. A photograph of the microscope including the corrector is shown in figure 6.1. Since the (electronic) setup of the corrector is not trivial we first make a few remarks about the steps needed to properly include the corrector in the beam path of the microscope. Next, we make a hypothesis about why no high-resolution images are obtained when the electron beam makes a roundtrip through the corrector. Experimental evidence is collected in support of this hypothesis. Finally, by considering when the signal at the sample plane reaches its maximum, we can precisely determine the voltages needed on the mirror electrodes to properly focus the electron beam on the CCP. These voltages are shown to agree very well with the values calculated previously, showing the MEMS fabricated mirrors are working as expected.

6.1 Aligning the Double Mirror Corrector

The steps needed to properly include the corrector in the beam path of the microscope are detailed in an alignment procedure which is considered too sensitive information to include in this thesis. Before including the corrector in the beam path of the microscope it is important to focus the beam on the CCP using the condenser lenses above the corrector. To achieve this focusing we make use of the optical model detailed in appendix A. While the corrector was in repair the optical model has been experimentally validated using a dummy column extension including a TEM grid, see figure 6.2. By focusing on the TEM grid while operating the microscope in beam align mode it was possible to find the condenser lens settings needed to place the crossover in the CCP. The experimentally found excitations agreed well with those predicted by the optical model (appendix A).

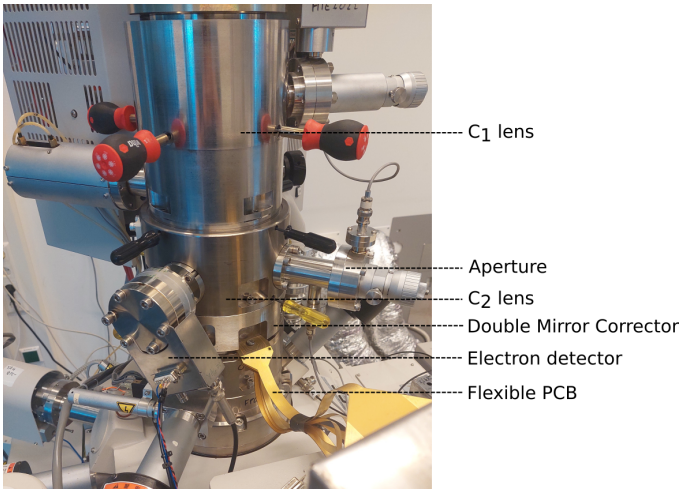

Figure 6.1: Photograph of the SU8030 microscope used for this research. The location of the DMC is shown in the image. The flexible printed circuit board (PCB) contains wires connecting the power supplies to the corrector. It can be seen the corrector can be integrated directly into a commercial electron microscope.

Once the electron beam is properly focused on the CCP using the condenser lenses, a number of different paths through the corrector have to be achieved before the corrector is fully operational. These paths are detailed in figure 6.3 and are named after the letter which resembles the shape of the path. Whenever the center of an electrostatic mirror or lens needs to be found we apply a large negative voltage to the corresponding electrode. This shrinks the size of the beam spot in beam align mode, allowing precise alignment to the center of the elements. It turns out that characteristic circular shapes appear whenever the electrostatic mirror or the bottom einzel lens is aligned using this method, see figure 6.4. As of yet the origin of these circular patterns is not understood, more research is needed to find the cause of these patterns.

The trickiest part in the proper alignment of the double mirror corrector is placing the electron beam centrally above the bottom mirror. If the top deflector excitation is not set properly the deflection of the EBE unit can still be changed to properly aim the electron beam through the center of the bottom mirror. This can give the operator of the corrector the illusion that the electron beam is focused properly above the center of the bottom mirror. Indirect evidence about the actual location of the crossover with respect to the bottom mirror can be obtained by considering whether the EBE unit sends the beam towards the center of the bottom einzel lens when the (electrostatic) deflection of the EBE unit is doubled. A moment of reflection should convince the reader that doubling the deflection of the EBE unit (transitioning from the Z path to the C path, see figure 6.3) can only send the electron beam through the center of the bottom deflector when the top deflector properly aims the beam above the center of the bottom mirror in the CCP.

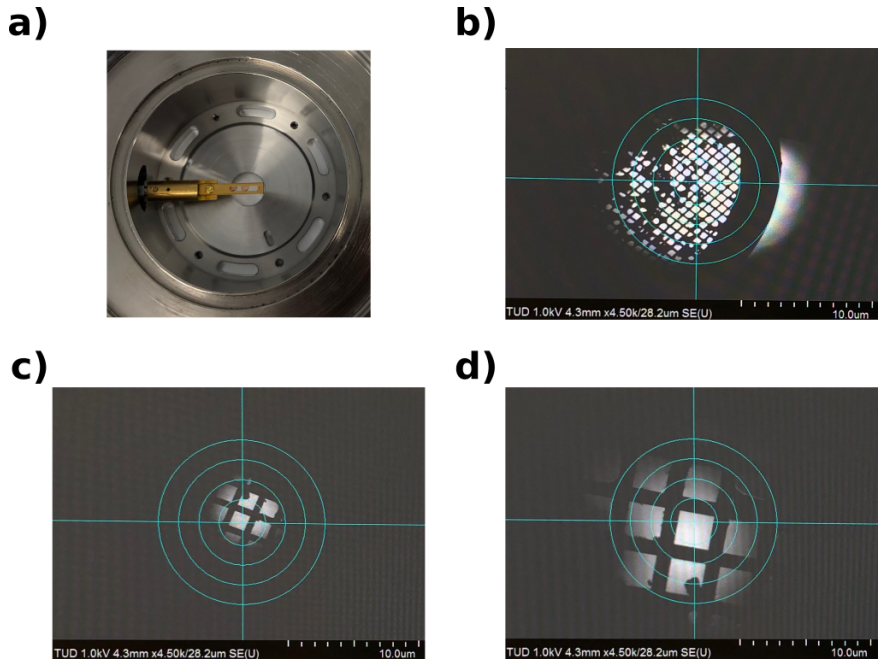

Figure 6.2: **a)** A column extension of the SU8030 microscope containing a TEM grid was used to validate the optical model detailed in appendix A. The grid is located at the same position as the common crossover plane in the corrector. By focusing on the grid while operating the microscope in beam alignment mode the lens strengths can be found that result in a crossover in the common crossover plane. **b)** Focusing with only condenser lens one. **c)** Focusing with only condenser lens two. **d)** Focusing with both condenser lenses one and two.

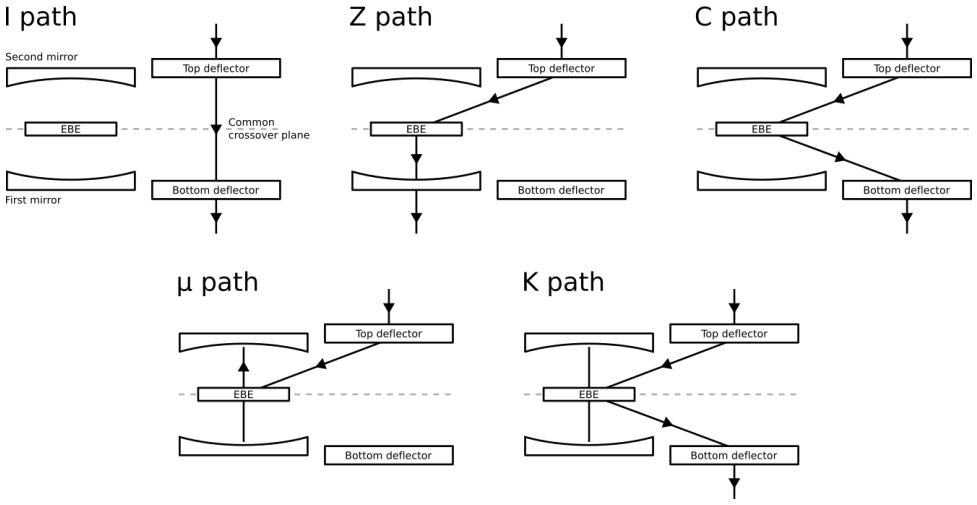

Figure 6.3: Possible paths the electron beam can take through the corrector. The paths are named after the letter which resembles the shape of the path. The Z and C paths can in theory be achieved both using electrostatic and magnetostatic deflections at the EBE unit. The μ and K paths need a combination of electrostatic and magnetostatic deflections (in the Wien condition) at the EBE unit. Terminology devised by Diederik J. Maas.

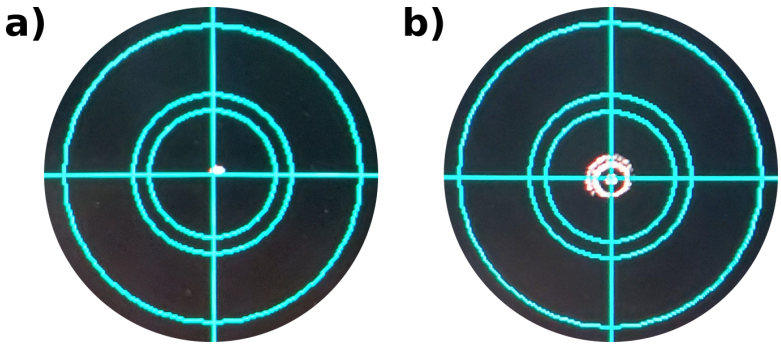

Figure 6.4: **a)** A large negative voltage of ~ 60% of the beam energy on the top einzel lens leads to a very small signal when scanning in the beam align mode. This allows to precisely align the electron beam through the center of the top einzel lens. **b)** A similarly large negative voltage on the bottom einzel lens leads to a characteristic circular pattern appearing around a small central dot. The origin of the circles is as of yet not understood.

6.2 Experimental verification of the required mirror voltages

Even though presently high-resolution images are not obtained when the beam travels through the K path (see figure 6.3), it is still possible to get secondary electron signal at the sample plane when using a larger magnetostatic deflection at the EBE unit. A larger magnetostatic deflection is unexpected but a possible cause is investigated in the next section. To validate the voltages found for the mirror geometry currently in the corrector (see figure 3.1) we consider when the signal at the sample plane is maximum. To ensure that the focal length of the mirror is correct in the experiment, we make sure the objective lens focuses the common crossover plane on the sample plane. Therefore, if the mirrors are capable of creating a reasonable crossover in the CCP the objective lens will focus the beam on the sample, thereby creating a large signal.

In the experiment, we apply a fixed voltage on the lens electrode and then adjust the mirror electrode voltage until the signal at the sample plane is maximized. The mean beam energy used is 1 keV. It turns out that the optimal mirror electrode voltage can be determined with an accuracy of 10 V. For the numerical calculation of the mirror voltages, we determine the distance from the CCP to either mirror electrode from the design files used to manufacture the corrector. This distance is not explicitely mentioned as it is considered sensitive information. A comparison between the experimentally determined mirror electrode voltages and the computed voltages can be seen in figure 6.5. The agreement between the calculations and the experimental values is very good, implying that the mirrors are working as expected.

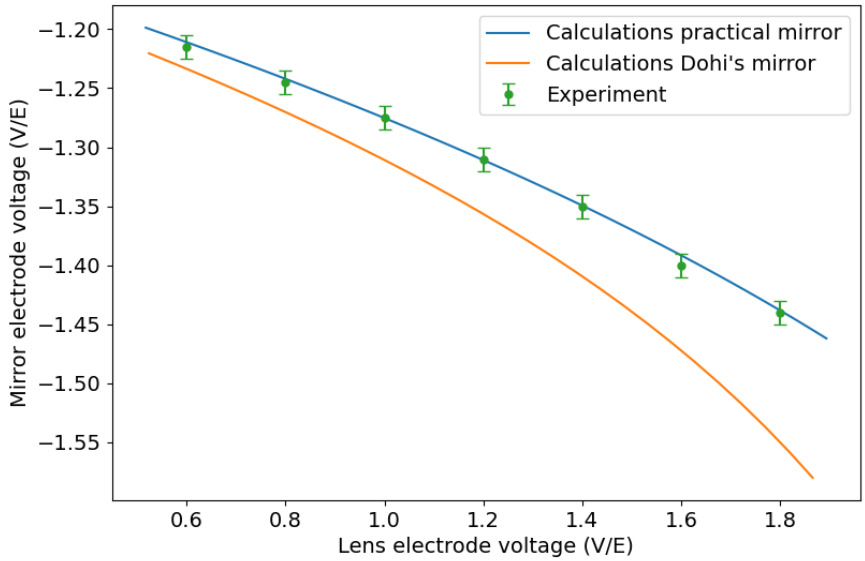

Figure 6.5: As explained in the text the mirror electrode voltages that cause proper focusing behavior in the CCP can be found by considering when the secondary electron signal at the sample plane reaches its maximum. The error bars are determined experimentally by considering the smallest change in mirror electrode voltage that has a visible effect on the signal strength. The experimental values are compared with calculations done for the mirror geometry shown in figure 3.1. The distance from the CCP to either mirror electrode is determined using the design files used to manufacture the corrector. The agreement between the calculations and the experimental values is very good. The excitation voltages (for the same focal length) for the mirror shown in figure 16 of [7] are also plotted. The geometry from [7] differs from the one shown in figure 3.1 in three important aspects. Firstly, for the mirror studied in this thesis [redacted] µm has been added to the spacing between the electrodes to account for two glue layers, making the space between the electrodes [redacted] µm. Secondly, the mirror electrode is not closed off at the bottom as it is in [7]. Finally, in figure 3.1 the influence of the grounded liner tube partially inserted into the grounded electrode has been taken into account.

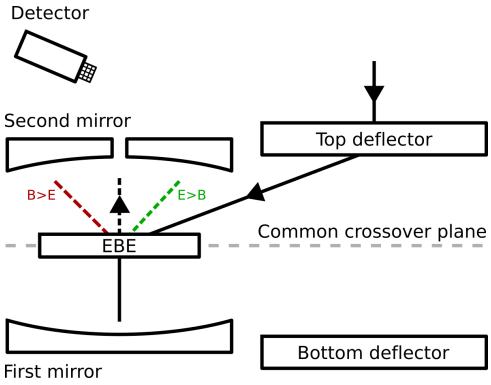

Figure 6.6: To quantify the lateral displacement of the top mirror with respect to the bottom mirror an experiment is devised in which the ratio of the electrostatic and the magnetostatic deflection at the EBE unit is varied. If the electrostatic and magnetostatic deflections are precisely balanced the electron beam experiences no deflection when traveling upward through the EBE unit. If the magnetostatic deflection is dominant the beam is deflected away from the microscope axis, while if the electrostatic deflection is dominant the beam is deflected towards the microscope axis. The top mirror stack is drawn with a central hole to remind us that the electron beam can pass through the center of the top mirror if the mirror electrodes are grounded (see figure 3.1).

6.3 Quantifying the lateral displacement of the top mirror

With the current version of the double mirror corrector, even when carefully aligning the system, no high resolution images can be obtained. It turns out that when the electron beam is properly centered above the bottom mirror and the deflection of the EBE unit is precisely divided between an electrostatic and a magnetostatic deflection, excitation of the bottom mirror is not enough to reflect the electron beam towards the top mirror. After some moments of deliberation, it was hypothesized that possibly the top mirror might be laterally displaced with respect to the bottom mirror. This would make the reflection from the bottom mirror miss the center of the top mirror, causing the electron beam to not reach the sample. The lateral displacement could be explained by an insufficient machining accuracy of the metal parts making up the corrector or from an unintentional displacement of either mirror while gluing the mirrors into the corrector.

To find support for this hypothesis an experiment is performed which is illustrated in figure 6.6. The ratio of electrostatic and magnetostatic deflection is varied while keeping the total deflection constant. This means that the electron beam is always deflected towards the center of the bottom mirror. The deflection experienced by the electron beam when traveling upwards through the EBE unit depends on the ratio of the magnetostatic deflection and the electrostatic deflection. If the deflection is dominated by the magnetostatic

deflection the upward deflection will be away from the microscope axis, while if the deflection is dominated by the electrostatic deflection the upward deflection will be towards the microscope axis. A secondary electron detector above the (non-excited) top mirror is used to determine for which upward deflection the electron beam travels through the center of the top mirror.

Using this procedure it was found that the magnetostatic deflection must be ~ 8 mrad larger than the electrostatic deflection to make the electron beam pass through the center of the top mirror. Multiplying this angle with the distance between the EBE unit and the mirror we find a misalignment of at least 100 µm. This lateral shift is much larger than the machining tolerances used to manufacture the corrector. More research is needed to understand the origin of this apparent misalignment and to ensure the conclusion from this experiment has not been influenced by the alignment of the top part of the electron microscope column.

7

Conclusion and outlook

The research and development of a DMC for a LVSEM has been advanced using numerical, mathematical and experimental results. When possible, model predictions have been verified experimentally. The mirrors integrated in the corrector have seen extensive modeling using a novel software library. This thesis contributes to the theoretical and numerical evidence that the DMC can be a valid and effective tool to improve the resolution of LV-SEMs.

The Python implementation of the BEM and the novel ray-tracing technique (section 2.2) have been used effectively to study the corrector. The ray-tracing techniques required the knowledge of the complicated expression for the higher-order derivatives of the axial potential. Fortunately, with the help of modern computer algebra systems this problem was overcome. The software has proven fast, accurate, and reliable and therefore warrants further development. Welcome additions to the software would be support for three-dimensional geometries, support for magnetostatic problems and more checks of the accuracy of the higher-order aberration coefficients. Documentation efforts to make the software usable to other researchers have already started.

The electrostatic mirror currently in the DMC has been thoroughly analyzed (figure 3.3) and the found excitation voltages have shown good agreement with the experiments (figure 6.5). The focal lengths of the mirror have been characterized for a wide range of lens and mirror electrode voltages thanks to the capability of the software to trace hundreds of thousands of electrons within reasonable time frames (figure 3.2). The characteristic shapes of the electron trajectories have been documented (figure 3.4) and it is argued that the magnitude of the aberrations correlate with the maximum distance from the optical axis of the trajectory. The mirror is shown to have negative chromatic and spherical aberrations, which allow us to overcome the obstacle formed by Scherzer's theorem. The higher-order aberration coefficients were shown to have a negligible impact on the ex-

pected beam angle and energy spread.

Next, we derived that the aberration coefficient C_{ij} scales with the object distance u and image distance v as $C_{ij} \propto u^i v$. This scaling behavior is also apparent in the previously computed figure 3.3. From a set of precomputed aberration coefficients at different focal lengths we can then use box 4.1.1 to compute the aberration coefficients at any given object and image distance. While the DMC should always be used with crossovers in the CCP, these mathematical results are still useful to predict how the aberrations change when the distance between the mirrors in the DMC is changed or to predict the deviation in the aberration coefficients when the position of the crossovers deviate from the CCP. The aberrations produced by the DMC are expressed in terms of the single mirror aberrations in formula 4.3, while the requirements for the DMC aberrations for aberration correction are summarized by formulas 4.6 and 4.7. It is found that independent of the magnifications of the lenses in the microscope, the DMC must fulfill the aberration matching condition 4.9 to allow for the simultaneous correction of the spherical and chromatic aberrations of the objective lens. Fortunately, the current design of the DMC is capable of providing all necessary matching condition values as shown in figure 4.4. Using the matching condition, a procedure is outlined in box 4.4.2 to achieve the simultaneous correction of chromatic and spherical aberrations. The aberration matching procedure uses the magnification of the bottom einzel lens to match the magnitudes of the aberrations produced by the DMC to those of the objective lens. The matching procedure 4.4.2 summarizes how the DMC should be operated.

Having completely characterized the mirror in the DMC and the correct operation of the DMC, we turned to possible improvements of the DMC in chapter 5. It is argued that the allowed beam energy, the sensitivity to misalignment, and the electrostatic interference from the grounded liner tunes are valid evaluation criteria to judge the quality of the electrostatic mirrors. These criteria are made quantitative and it is shown that the distance between the lens and mirror electrode and the radius of the aperture in the mirror electrode have a large effect on the evaluation criteria. In contrast, the radius of the aperture in the lens electrode and the distance between the ground and lens electrode have very little influence on the evaluation criteria. Using the evaluation criteria as a guide a new triode mirror design was proposed which improved upon the sensitivity to misalignment and the maximum allowed beam energy. Furthermore, a tetrode mirror design was systematically studied by considering the evaluation criteria as a function of the voltage on the auxiliary electrode, the result of which is shown in figure 5.6.

Despite efforts to carefully align the microscope and the DMC, the current version of the corrector is not yet capable of generating high-resolution images. It was hypothesized that the problem was a misalignment between the two mirrors in the corrector, and experimental evidence was collected indicating the misalignment to be more than 100 µm. This misalignment is larger than the machining tolerances used to manufacture the corrector, causing doubts about the validity of this conclusion. More research is needed to understand the origin of this misalignment and to ensure the conclusion from this experiment has not been influenced by the alignment of the top part of the electron microscope

column. The lack of high-resolution images have so far prevented the experimental determination of the aberrations produced by the DMC. Still, it has been possible to establish the relevant excitation voltages of the electrostatic mirrors and these are shown in figure 6.5 to match very well with the calculated voltages. This shows the electrostatic mirrors themselves are working as expected up to at least the first order optical properties. To complete the experimental validation of the electrostatic mirrors their spherical and chromatic aberrations should be measured.

The main obstacle in the experimental setup has so far been the difficulty of getting the entire beam through the K-path down to the sample plane (see figure 6.3). Further research on the DMC should therefore focus on determining the exact place in the corrector where beam current is lost. A new design of the DMC should make alignment and achieving K-path with full current at the sample plane easier. To achieve this, the dimensions of the electrodes in the DMC should be scaled up and the distance between the mirror and microscope axis should be enlarged. This ensures that we are less sensitive to manufacturing (and gluing) tolerances. An increase in deflection aberrations is not expected if the height of the DMC is scaled up proportionately with the distance between the microscope and mirror axis, since in that case the deflection angles would stay equal. The magnitude of the aberrations of the mirror will increase with the height of the DMC (equation 4.2) but this effect can be negated by increasing the distance between the lens and mirror electrode or increasing the mirror radius (figure 5.4).

In terms of modeling, it would be beneficial to know the origin of the circular patterns visible when the microscope is operating in beam align mode (figure 6.4). Understanding of these features would allow us to conclude whether using them for alignment is a valid approach. Furthermore, the exact resolution loss of the DMC as a result of deflection aberrations needs to be quantified more precisely than done previously [7]. For this purpose support for simulating planar symmetric geometries is being added to the software library used for this thesis. This allows computation of the aberrations of the electrostatic deflectors. Knowledge of the exact resolution loss caused by the deflection aberrations would allow us to determine the maximum tolerable deflection angles in the DMC.

A

Optical model of the extended SU8030 microscope

To achieve aberration correction it is paramount to have sufficiently detailed control and understanding of the operating conditions of the microscope. For this reason, an optical model was built that models the operation of the commercial SU8030 microscope[1]. The optical model consists of a Python user interface that allows the user to interactively change the configuration of the microscope. The application is shown in figure A.1.

Features implemented

The optical model allows the user to vary the lens strength of the relevant lenses. Automatically the angular magnification $M_\alpha = \frac{u}{v}$ is computed for each lens from the configured object distance u and image distance v. The angular magnifications are used to calculate the beam angle at any point in the microscope. The location and size of the aperture is properly taken into account when calculating the beam angles. Lenses can also be turned off in the model to allow the user to explore different modes in which the microscope can be operated.

The virtual displacement of the electron source for different extractor voltages has also been included in the model. The user can copy the settings from the Hitachi user interface into the model and consider the current state of the microscope. The aberration curves of the electrostatic mirrors for a number of different focal lengths have been precomputed using the BEM and are read into the model at startup. Using box 4.1.1 and equation 4.3 this allows the instantaneous computation of the chromatic and spherical aberration of either mirror and the entire corrector.

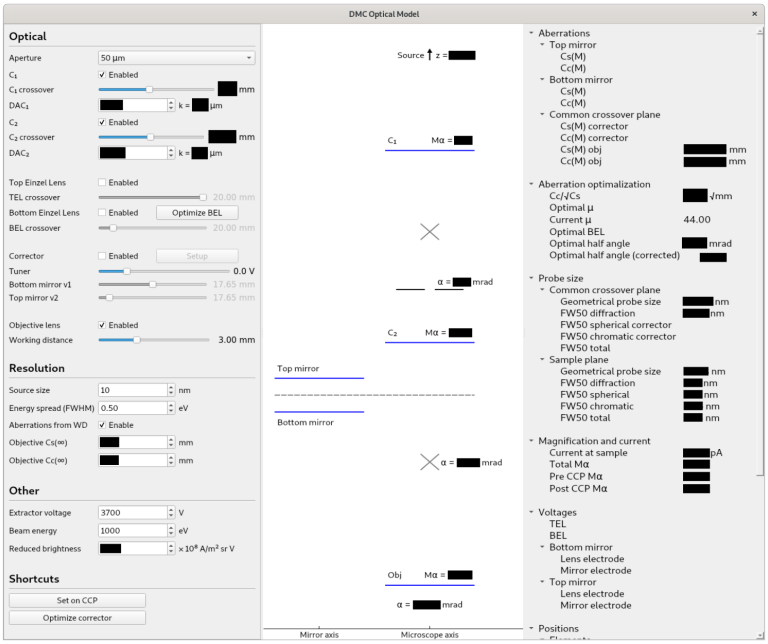

Figure A.1: The user interface of an optical model which characterizes the operation of the SU8030 Hitachi microscope. The user interface is interactive and allows the user to setup the DMC for optimal aberration correction. The many features included in the model are mentioned in the main text. The 'optimize corrector' button shown in the bottom left can be used to automatically complete the aberration matching procedure (box 4.4.2). The optical model has seen experimental verification, see table A.1. Random offsets are added to the lens positions in the screenshot to not leak their relative position.

The procedure for achieving simultaneous correction of both the lowest order chromatic and spherical aberrations (box 4.4.2) has been implemented in the model and can be completed by a click of a button. This means that the optimal voltages of the electrostatic mirrors are automatically calculated for the current working conditions of the microscope. To judge the resolution improvement achieved it is important to know the probe size at the sample plane both before and after correction. The probe size at the sample plane is calculated using the following formula [40]:

$$d_{\mathrm{FW50}} = \left(\left(\left(d_I^{1.3} + \left((d_A^4 + d_S^4)^{\frac{1}{4}} \right)^{1.3} \right)^{\frac{1}{1.3}} \right)^2 + d_c^2 \right)^{\frac{1}{2}}$$

where d_{FW50} is the probe size containing 50% of the beam current. d_I, d_A, d_S, and d_c are the contributions to the probe size from the source image, the diffraction disc, the spherical

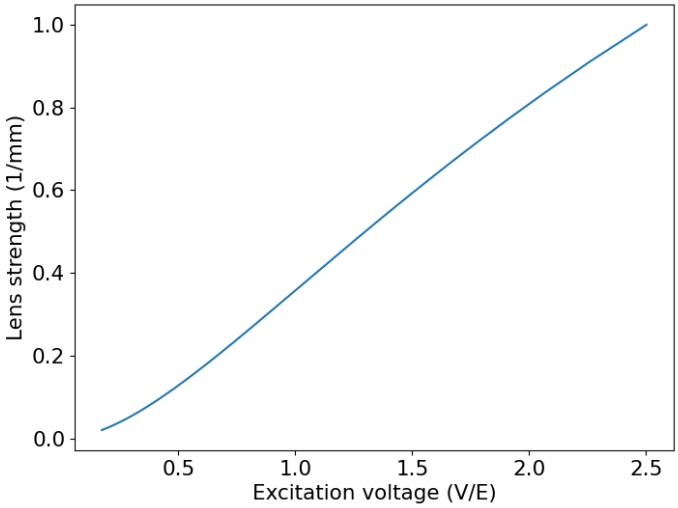

Figure A.2: Lens strength $k = 1/f$ of the bottom einzel lens and top einzel lens as a function of the excitation voltage. The lenses are MEMS fabricated and consist of 500 µm thick electrodes. The insulating spacers between the electrodes are 500 µm but ■ µm has been added to the spacing to account for two glue layers.

aberration and the chromatic aberration, respectively. The formulas to calculate these contributions can be found in [7, 39, 40]. The geometrical probe size can be calculated from the source size d_v and the total magnification of the system using $d_I = Md_v$. Using formula 2.2 from [39] we can then calculate the current at the sample plane using

$$I_p = B_r \frac{\pi}{4} d_I^2 \pi \alpha^2 V$$

where B_r is the reduced brightness of the electron source, α is the beam semi-angle, and V is the accelerating voltage at the target.

The top einzel lens and bottom einzel lens are also included in the model. The relationship between the einzel lens excitation voltage and the lens strength has been found using the boundary element method described in chapter 2, see figure A.2. The optical model displays the necessary excitation voltage of the einzel lenses when they are enabled in the user interface.

Experiment	Lenses used
Focus on sample plane	Only C1
Focus on sample plane	Only C2
Focus on aperture	Only C1
Focus on TEM grid in CCP	Only C1
Focus on TEM grid in CCP	Only C2
Focus on TEM grid in CCP	C1 and C2, at different lens strengths

Table A.1: List of experimental verifications done with the optical model to ensure the computed lens strengths are correct. During a repair procedure of the microscope, a dummy column extension was installed with the capability of inserting a TEM grid at the CCP, which offered another important location to focus on, see figure 6.2. The predicted DAC values were compared with the experimentally found values and the predicted values were always within the measurement error of the experiment. The actual DAC values and lens strengths found are omitted to not leak any sensitive information of HHT about the SU8030.

Experimental verification

The optical model has seen experimental verification. A list of different verifications done with the optical model to ensure the validity of its predictions is shown in table A.1. To find the lens strengths of the condenser lenses which result in a crossover in the CCP a column extension containg a TEM grid was used, see figure 6.2. The list of corresponding DAC values and lens strengths is not shown since this is considered sensitive information of HHT. We do however note that the deviation in the predicted crossover positions and the measured positions was always within the measurement error of the experiment. This validates the predictions made by the model.

Acknowledgments

First and foremost I would like to thank Diederik Maas for his guidance during the project, his elaborate feedback on draft versions of this thesis, and for teaching me how to handle a modern SEM. I would also like to thank Pieter Kruit for his supervision, fruitful discussions, and for creating a research environment in which I could be productive as a starting scientist. I would like to thank Sergey Loginov for supervision when working with an alternative experimental setup. Furthermore, I would like to thank Han van der Linden, Carel Heerkens, Ruud van Tol, Youp van Goozen and Johan van der Cingel for their work on the experimental setup. I would also like to express my gratitude to Ali Mohammadi Gheidari and Florian Bociort for being part of my assessment committee. Finally, I would like to thank Hitachi High-Tech Corporation (HHT) and especially Kazumi-san for their collaboration on this project[1].

Bibliography

[1] MAR Krielaart et al. "Miniature electron beam separator based on three stacked dipoles". In: *Journal of Applied Physics* 127.23 (2020), p. 234904.

[2] G. Moore. "Cramming more components onto integrated circuits". In: *Electronics Magazine* (1965).

[3] Benjamin Bunday et al. "Photoresist shrinkage effects in 16 nm node extreme ultraviolet (EUV) photoresist targets". In: *Metrology, Inspection, and Process Control for Microlithography XXVII*. Ed. by Alexander Starikov and Jason P. Cain. Vol. 8681. International Society for Optics and Photonics. SPIE, 2013, pp. 173–187. DOI: 10.1117/12.2012470. URL: https://doi.org/10.1117/12.2012470.

[4] Benjamin Bunday et al. "CD-SEM metrology for sub-10nm width features". In: *Metrology, Inspection, and Process Control for Microlithography XXVIII*. Ed. by Jason P. Cain and Martha I. Sanchez. Vol. 9050. International Society for Optics and Photonics. SPIE, 2014, pp. 238–257. DOI: 10.1117/12.2047099. URL: https://doi.org/10.1117/12.2047099.

[5] O. Scherzer. "Über einige fehler von elektronenlinsen". In: *Zeitschrift für Physik* 101.9-10 (1936), pp. 593–603.

[6] O. Scherzer. "Spharische und chromatische korrektur von elektronen-linsen". In: *Optik* 2 (1947), pp. 114–132.

[7] Hideto Dohi and Pieter Kruit. "Design for an aberration corrected scanning electron microscope using miniature electron mirrors". In: *Ultramicroscopy* 189 (2018), pp. 1–23.

[8] Harald H. Rose. "Historical aspects of aberration correction". In: *Journal of Electron Microscopy* 58.3 (Mar. 2009), pp. 77–85. ISSN: 0022-0744. DOI: 10.1093/jmicro/dfp012. eprint: https://academic.oup.com/jmicro/article-pdf/58/3/77/5854538/dfp012.pdf. URL: https://doi.org/10.1093/jmicro/dfp012.

[9] Maximilian Haider et al. "Towards 0.1 nm resolution with the first spherically corrected transmission electron microscope". English (US). In: *Microscopy (Oxford, England)* 47.5 (1998), pp. 395–405. ISSN: 2050-5698. DOI: 10.1093/oxfordjournals.jmicro.a023610.

[10] O.L. Krivanek et al. "Towards sub-0.5Å electron beams". In: *Ultramicroscopy* 96.3 (2003). Proceedings of the International Workshop on Strategies and Advances in Atomic Level Spectroscopy and Analysis, pp. 229–237. ISSN: 0304-3991. DOI: 10.1016/S0304-3991(03)00090-1. URL: https://www.sciencedirect.com/science/article/pii/S0304399103000901.

[11] Joachim Zach and Maximilian Haider. "Aberration correction in a low voltage SEM by a multipole corrector". In: *Nuclear Instruments and Methods in Physics Research Section A: Accelerators, Spectrometers, Detectors and Associated Equipment* 363.1 (1995). Charged Particle Optics, pp. 316–325. ISSN: 0168-9002. DOI: 10.1016/0168-9002(95)00056-9. URL: https://www.sciencedirect.com/science/article/pii/0168900295000569.

[12] D.J. Maas and E.G.T. Bosch. *Alignment cookbook for the Electrostatic Corrector prototype Mark-II*. Tech. rep. Philips Research Eindhoven, 2006.

[13] Shinobu Uno et al. "Aberration correction and its automatic control in scanning electron microscopes". In: *Optik* 116.9 (2005), pp. 438–448. ISSN: 0030-4026. DOI: 10.1016/j.ijleo.2005.03.001. URL: https://www.sciencedirect.com/science/article/pii/S0030402605000859.

[14] Kotoko Hirose, Tomonori Nakano, and Takeshi Kawasaki. "Automatic aberration-correction system for scanning electron microscopy". In: *Microelectronic Engineering* 88.8 (2011). Proceedings of the 36th International Conference on Micro- and Nano-Engineering (MNE), pp. 2559–2562. ISSN: 0167-9317. DOI: 10.1016/j.mee.2010.12.040. URL: https://www.sciencedirect.com/science/article/pii/S0167931710005289.

[15] A. Khursheed and W. K. Ang. "On-Axis Electrode Aberration Correctors for Scanning Electron/Ion Microscopes". In: *Microscopy and Microanalysis* 21.S4 (2015), pp. 106–111. DOI: 10.1017/S1431927615013227.

[16] R.H van Aken et al. "Low-energy foil aberration corrector". In: *Ultramicroscopy* 93.3 (2002). Special issue in Honour of Peter W. Hawkes on the Occasion of his 65th Birthday, in Recognition of his Contributions to Electron Optics and Electron Microscopy, pp. 321–330. ISSN: 0304-3991. DOI: 10.1016/S0304-3991(02)00287-5. URL: https://www.sciencedirect.com/science/article/pii/S0304399102002875.

[17] R.H. van Aken et al. "Design of an aberration corrected low-voltage SEM". In: *Ultramicroscopy* 110.11 (2010), pp. 1411–1419. ISSN: 0304-3991. DOI: 10.1016/j.ultramic.2010.07.012. URL: https://www.sciencedirect.com/science/article/pii/S0304399110002123.

[18] Zhifeng Shao and Xiao Dong Wu. "Properties of a four-electrode adjustable electron mirror as an aberration corrector". In: *Review of Scientific Instruments* 61.4 (1990), pp. 1230–1235. DOI: 10.1063/1.1141216. eprint: https://doi.org/10.1063/1.1141216. URL: https://doi.org/10.1063/1.1141216.

[19] J.P.S. Fitzgerald, R.C. Word, and R. Könenkamp. "Simultaneous and independent adaptive correction of spherical and chromatic aberration using an electron mirror and lens combination". In: *Ultramicroscopy* 115 (2012), pp. 35–40. ISSN: 0304-3991. DOI: 10.1016/j.ultramic.2012.02.001. URL: https://www.sciencedirect.com/science/article/pii/S0304399112000320.

[20] Jack C. Straton. "Analytic solution for a quartic electron mirror". In: *Ultramicroscopy* 148 (2015), pp. 168–179. ISSN: 0304-3991. DOI: 10.1016/j.ultramic.2014.09.003. URL: https://www.sciencedirect.com/science/article/pii/S0304399114001740.

[21] Gertrude F. Rempfer. "A theoretical study of the hyperbolic electron mirror as a correcting element for spherical and chromatic aberration in electron optics". In: *Journal of Applied Physics* 67.10 (1990), pp. 6027–6040. DOI: 10.1063/1.345212. eprint: https://doi.org/10.1063/1.345212. URL: https://doi.org/10.1063/1.345212.

[22] R. Fink et al. "SMART: a planned ultrahigh-resolution spectromicroscope for BESSY II". In: *Journal of Electron Spectroscopy and Related Phenomena* 84.1 (1997), pp. 231–250. ISSN: 0368-2048. DOI: 10.1016/S0368-2048(97)00016-9. URL: https://www.sciencedirect.com/science/article/pii/S0368204897000169.

[23] Gertrude F. Rempfer et al. "Simultaneous Correction of Spherical and Chromatic Aberrations with an Electron Mirror: An Electron Optical Achromat". In: *Microscopy and Microanalysis* 3.1 (1997), pp. 14–27. DOI: 10.1017/S143192769797001X.

[24] H. Müller, D. Preikszas, and H. Rose. "A beam separator with small aberrations". In: *Journal of Electron Microscopy* 48.3 (Jan. 1999), pp. 191–204. ISSN: 0022-0744. DOI: 10.1093/oxfordjournals.jmicro.a023670. eprint: https://academic.oup.com/jmicro/article-pdf/48/3/191/2573064/48-3-191.pdf. URL: https://doi.org/10.1093/oxfordjournals.jmicro.a023670.

[25] Th. Schmidt et al. "Double aberration correction in a low-energy electron microscope". In: *Ultramicroscopy* 110.11 (2010), pp. 1358–1361. ISSN: 0304-3991. DOI: 10.1016/j.ultramic.2010.07.007. URL: https://www.sciencedirect.com/science/article/pii/S030439911000207X.

[26] R.M. Tromp et al. "A new aberration-corrected, energy-filtered LEEM/PEEM instrument. I. Principles and design". In: *Ultramicroscopy* 110.7 (2010), pp. 852–861. ISSN: 0304-3991. DOI: 10.1016/j.ultramic.2010.03.005. URL: https://www.sciencedirect.com/science/article/pii/S0304399110000835.

[27] R.M. Tromp et al. "A new aberration-corrected, energy-filtered LEEM/PEEM instrument II. Operation and results". In: *Ultramicroscopy* 127 (2013). Frontiers of Electron Microscopy in Materials Science, pp. 25–39. ISSN: 0304-3991. DOI: 10.1016/j.ultramic.2012.07.016. URL: https://www.sciencedirect.com/science/article/pii/S0304399112001866.

[28] MAR Krielaart. "Electron wave front modulation with patterned mirrors". PhD thesis. Delft University of Technology, 2021.

[29] MAR Krielaart and P Kruit. "Flat electron mirror". In: *Ultramicroscopy* 220 (2021), p. 113157.

[30] M Oral and B Lencová. "Calculation of aberration coefficients by ray tracing". In: *Ultramicroscopy* 109.11 (2009), pp. 1365–1373.

[31] D. R. Cruise. "A Numerical Method for the Determination of an Electric Field about a Complicated Boundary". In: *Journal of Applied Physics* 34.12 (1963), pp. 3477–3479. DOI: 10.1063/1.1729242. eprint: https://doi.org/10.1063/1.1729242. URL: https://doi.org/10.1063/1.1729242.

[32] A Renau, F H Read, and J N H Brunt. "The charge-density method of solving electrostatic problems with and without the inclusion of space-charge". In: *Journal of Physics E: Scientific Instruments* 15.3 (Mar. 1982), pp. 347–354. DOI: 10.1088/0022-3735/15/3/025. URL: https://doi.org/10.1088/0022-3735/15/3/025.

[33] David Edwards. "Accurate potential calculations for the two tube electrostatic lens using a multiregion FDM method". In: *EUROCON 2007-The International Conference on" Computer as a Tool"*. IEEE. 2007, pp. 1960–1969.

[34] Peter W Hawkes and Erwin Kasper. *Principles of electron optics*. Vol. 1. Academic press, 2018. Chap. 7.

[35] Erwin Fehlberg. "Low-Order Classical Runge-Kutta Formulas With Stepsize Control and their Application to Some Heat Transfer Problems". In: (1969).

[36] D Cubric et al. "Comparison of FDM, FEM and BEM for electrostatic charged particle optics". In: *Nuclear Instruments and Methods in Physics Research Section A: Accelerators, Spectrometers, Detectors and Associated Equipment* 427.1 (1999), pp. 357–362. ISSN: 0168-9002. DOI: 10.1016/S0168-9002(98)01563-0. URL: https://www.sciencedirect.com/science/article/pii/S0168900298015630.

[37] D. Preikszas and H. Rose. "Correction properties of electron mirrors". In: *Journal of Electron Microscopy* 46.1 (Jan. 1997), pp. 1–9. ISSN: 0022-0744. DOI: 10.1093/oxfordjournals.jmicro.a023484. eprint: https://academic.oup.com/jmicro/article-pdf/46/1/1/2515917/46-1-1.pdf. URL: https://doi.org/10.1093/oxfordjournals.jmicro.a023484.

[38] H. Rose and D. Preikszas. "Time-dependent perturbation formalism for calculating the aberrations of systems with large ray gradients". In: *Nuclear Instruments and Methods in Physics Research Section A: Accelerators, Spectrometers, Detectors and Associated Equipment* 363.1 (1995). Charged Particle Optics, pp. 301–315. ISSN: 0168-9002. DOI: 10.1016/0168-9002(95)00065-8. URL: https://www.sciencedirect.com/science/article/pii/0168900295000658.

[39] Pieter Kruit. *Introduction to Charged Particles Optics*. 2020.

[40] JE Barth and P Kruit. "Addition of different contributions to the charged particle probe size". In: *Optik* 101.3 (1996), pp. 101–109. ISSN: 0030-4026.